

# Chapter 8

## Raven: Developing a Surgical Robot from a Concept to a Transatlantic Teleoperation Experiment

Jacob Rosen, Mitchell Lum, Mika Sinanan, and Blake Hannaford

### 8.1 Introduction

For decades surgery and robotics were progressing along two parallel paths. In surgery, minimally invasive surgery (MIS) revolutionized the way a significant number of surgical interventions were performed. Minimally invasive surgery allows the surgeon to make a few small incisions in the patient, rather than making one large incision for access. This technique allows for significantly faster recovery times, less trauma, and decreased pain medication requirements for the patient.

In robotics, teleoperation integrated the human into robotic systems. Only in the last decade have surgery and robotics reached a level of maturity that allowed safe assimilation between the two in a teleoperation mode for creating a new kind of operating room with the potential for surgical innovation long into the future [1].

A detailed historical overview of surgical robotics is beyond the scope of this chapter. The reader may refer to several published papers, which collectively may provide a comprehensive survey of the field of surgical robotics and its applications in various sub-disciplines of surgery and medicine [2–17]. The remaining of this section will provide a brief overview of key systems and milestones of the research activities in the field of surgical robotics and telesurgery.

One of the earliest applications of robotics in surgery in mid 1980s included a modified Puma 560 which was used as a positioning device to orient a needle for biopsy of the brain on a 52 year-old male [18]. In parallel research efforts at IBM were focused on a bone cutting robot with clinical application in total hip-replacement – a system later known as the ROBODOC [19]. The late 1980s also brought on a revolution in surgical intervention. Jacques Ferrisat, MD, from Bordeaux, France presented a

---

© 2006 IEEE. Mitchell J.H. Lum, Jacob Rosen, M.N. Sinanan, Blake Hannaford, Optimization of Spherical Mechanism for a Minimally Invasive Surgical Robot: Theoretical And Experimental Approaches”, IEEE Transactions on Biomedical Engineering Vol. 53, No. 7, pp. 1440–1445, July 2006

J. Rosen (✉)

Department of Computer Engineering, Jack Baskin School of Engineering,  
University of California Santa Cruz, 1156 High Street, Santa Cruz, CA 95064, USA  
e-mail: rosen@ucsc.edu

video clip at SAGES (Society of American Gastrointestinal Endoscopic Surgeons) of the first laparoscopic cholecystectomy (gall bladder removal). Minimally invasive surgery techniques greatly influenced the approaches that roboticists have taken toward robot assisted interventions. These key events set the stage for an introduction of surgical robotics into a clinical setup.

Two ground braking systems were developed in academia in the mid to late 1990s both using a four bar mechanism: the *Silver and the Black Falcon* [20] and the *Laparoscopic Telesurgery Workstation* [21]. Intuitive Surgical Inc. and Computer Motion Inc. both produced commercially available FDA-approved surgical robot systems for MIS. Computer Motion's Zeus surgical robot held a surgical tool on a SCARA-type manipulator. The Intuitive Surgical Inc. da Vinci R uses an extended parallel 4-bar mechanism. The deVinci synthesized two sub systems: (1) The surgeon console (master) including a 3D vision was originally developed by SRI as part of a system known as the M7 – A surgical robot for open surgery; (2) the surgical robot itself along with the wristed tools were based on the Black Falcon developed by MIT. In 2003, after years of litigation and counter-litigation over intellectual property rights, the two companies merged under the name Intuitive Surgical Inc. (ISI). There are currently several hundreds da Vinci systems in use throughout the world.

Telesurgery on a human patient was accomplished on September 9, 2001 by Marescaux and Gagner. In collaboration with Computer Motion, they used a modified Zeus system to teleoperate between New York City and Strasbourg, France under a 155 ms time delay using a dedicated Asynchronous Transfer Mode (ATM) communication link [22, 23]. Several key non-clinical teleoperation experiments were conducted with both the RAVEN, and the M7 in extreme environment (desert, underwater, and zero gravity) demonstrated the capabilities of surgical robotic systems to deliver surgical expertise along large distance with a combination of wired and wireless communication [24–27].

In Asia, a group from the University of Tokyo has recently been working on a new telesurgery system [19, 28], and has completed laparoscopic cholecystectomy on a porcine model between sites in Japan, and more recently between Japan and Thailand [1, 2]. In Europe, the Laboratoire de Robotique de Paris at University of Paris, (LRP) uses a spherical mechanism similar to the RAVEN. This robot moves the port in addition to the tool. This allows to embed force sensors in the device that give a direct reading of the forces at the tool tip, instead of the combined interaction forces of the tool/tissue and trocar/abdomen.

The Light Endoscopic Robot (LER) was developed at the University of Hawaii, Manoa. This device was designed to guide an endoscopic camera, but is now capable of holding disposable endoscopic graspers as well as a tool with wrist articulation [29, 30].

The following chapter describes the research efforts lasted for more the a decade in developing a fully operational surgical robot – the RAVEN, based on a profound collaboration between surgeons and engineers. It will cover: (1) the surgical specification of the system that was based on quantitative measurements in an animal lab as well as the operating room (2) the mechanism kinematic optimization based on these specs; (3) the system integration efforts; and (4) the experimental results of system performance in multiple field and lab experiments of teleoperation under time delay.

## 8.2 Design of the Surgical Robot

### 8.2.1 Clinical Requirements

The Blue Dragon is a passive device instrumented with sensors that are capable of measuring the surgical tool position and orientation in space, along with the forces, and torques applied on the minimally invasive tools by the surgeon hands and the corresponding tissues (Fig. 8.1). Using the Blue Dragon, an extensive database was collected of in-vivo tissue handling/examination, dissection, and suturing tasks performed by 30 surgeons operating on a swine models [31–36]. The data is summarized in Table 8.1.

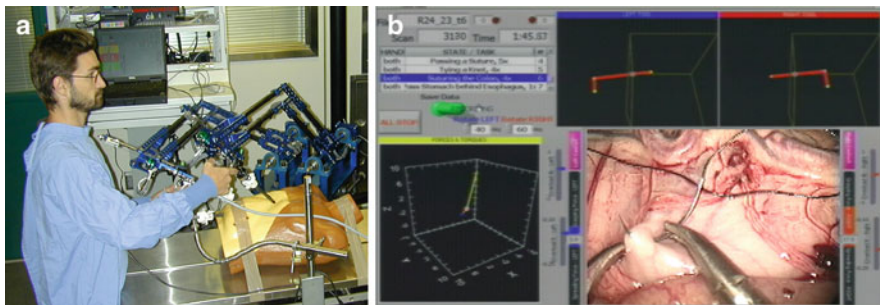


**Fig. 8.1** The Blue Dragon system: (a) The system integrated into a minimally invasive surgery operating room. (b) Graphical user interface

**Table 8.1** Design requirements based on in-vivo surgical measurement. Reference frames oriented such that x-axis points superior/inferior, y-axis is lateral/medial, z-axis straight up

Quantity	Symbol	Units	Value
Position/orientation	$\Delta\theta_x$	[Deg]	53.80
	$\Delta\theta_y$	[Deg]	36.38
	$\Delta\theta_z$	[Deg]	148.09
	$\Delta R$	[m]	0.1027
	$\Delta\theta_g$	[Deg]	24.08
	$\Delta X$	[m]	0.1026
	$\Delta Y$	[m]	0.0815
	$\Delta Z$	[m]	0.0877
Velocity	$\omega_x$	[rad/s]	0.432
	$\omega_y$	[rad/s]	0.486
	$\omega_z$	[rad/s]	1.053
	$V_r$	[M/s]	0.072
	$\omega_g$	[rad/s]	0.0468
Peak force	$F_x$	[N]	14.729
	$F_y$	[N]	13.198
	$F_z$	[N]	67.391
	$F_g$	[N]	41.608
Torque	$T_x$	[Nm]	2.394
	$T_y$	[Nm]	1.601
	$T_z$	[Nm]	0.0464

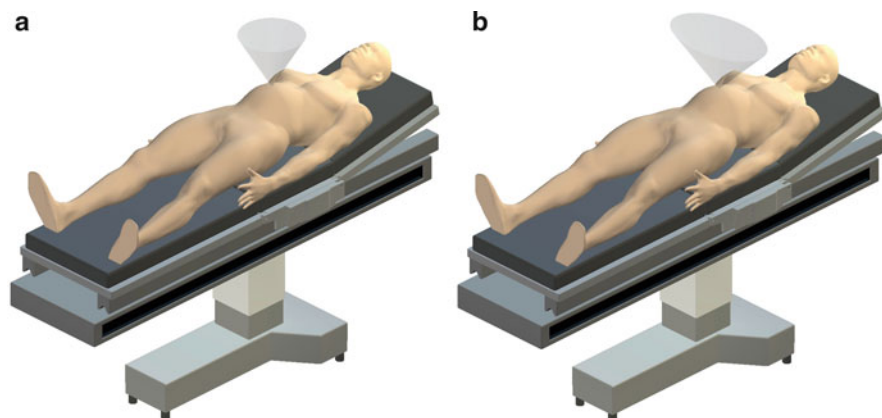


**Fig. 8.2** Workspace definitions of the surgical robot in MIS (a) dexterous workspace – High dexterity region defined by a right circular cone with a vertex angle of  $60^\circ$  and contains 95% of the tool motions based on in-vivo measurements. (b) Extended Dexterous Work Space – An elliptical cone with a vertex angle of  $60\text{--}90^\circ$  represents the reachable workspace such that any organ in the abdomen can be reached by the endoscopic tool

Analysis of this data indicated that, 95% of the time, the surgical tools were located within a conical range of motion with a vertex angle of  $60^\circ$  (termed the dexterous workspace, DWS). A measurement taken on a human patient showed that, in order to reach the full extent of the abdomen, the tool needed to move  $90^\circ$  in the mediolateral (left to right) and  $60^\circ$  in the superior/inferior direction (head to foot) – Fig. 8.2a. The extended dexterous workspace (EDWS) was defined as a conical range of motion with a vertex angle of  $90^\circ$  and is the workspace required to reach the full extent of the human abdomen without reorientation of the base of the robot – Fig. 8.2b. These parameters, obtained through surgical measurement, served as a basis for the kinematic optimization of the RAVEN spherical mechanism [15, 18].

## 8.2.2 Kinematics of a Spherical Mechanism

### 8.2.2.1 Description of the Mechanism and Frame Assignments

In the class of spherical mechanisms, all links' rotation and translation axes intersect at a signal point or at infinity, referred to as the mechanism's remote center of rotation. Locating the remote center at the tool's point of entry to the human body through the surgical port, as typically done in minimally invasive surgery (MIS), constitutes a point in space where the surgical tool may only rotate around it but not translated with respect to it. The selected spherical mechanism has two configurations in the form of parallel (5R – Fig. 8.3a) and serial (2R – Fig. 8.3b) configurations. The parallel mechanism is composed of two serial arms: Arm 1 – Link13 and Link35 and Arm 2 – Link24 and Link46 joined by a stationary base defined by Link12 through Joints

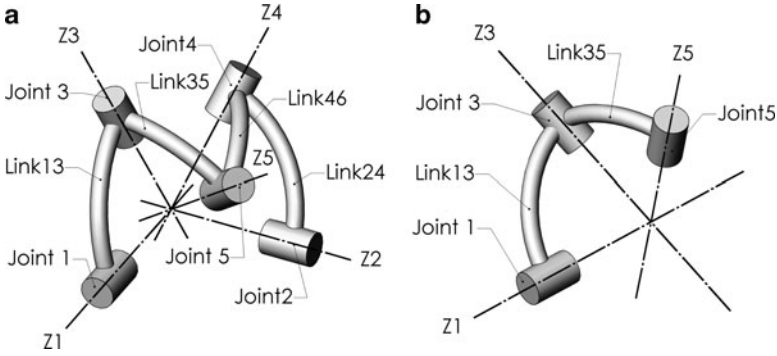


**Fig. 8.3** Spherical mechanism – link and joint coordinate frame assignment (a) Parallel Manipulator (b) Serial Manipulator

1 and 2. The parallel chain is closed at the two collinear joints, 5 and 6. Arm 1 and 2 will be further referred to as the even and odd side of the parallel manipulator respectively. The spherical serial mechanism includes only one arm (Arm 1) with the same notation as the odd side of the parallel mechanism. By definition, the links of both mechanisms are moving along the surface of a sphere with an arbitrary radius  $R$ . All the rotation axes of the links intersect at the center of the sphere. The kinematic analysis is independent of the sphere’s radius, however, from a practical perspective; the radius of the sphere should be kept as small as possible to minimize the overall size of the mechanism and the dynamic effects. As configured for MIS, the end-effector of the mechanism is inserted through Joint 5. Both the parallel and serial configurations are considered a 2-DOF mechanism. Any two joint angles determine the orientation of the end-effector in space; we chose  $\theta_1$  and  $\theta_2$  in the parallel configuration and by  $\theta_1$  and  $\theta_3$  in the serial configuration. For the purpose of kinematic analysis, the center of the sphere serves as the origin for all reference frames of the mechanism’s links. Thus, the transformations between the mechanism links’ coordinate frames can be expressed as pure rotations.

Following the Denavit–Hartenberg (D–H) frame assignment convention (Table 8.2), frames are assigned to the mechanism joints such that the Z-axis of the  $n$ th frame points outward along the  $n$ th joint [28]. Following the numbering scheme set for by Ouerfelli and Kumar [25] the frames have odd numbers along Arm1 (Frames 0', 1, 3 and 5) and even numbers along Arm2 (Frame 0'', 2, 4 and 6) – see Fig. 8.2a. The end-effector frame is Frame 5. Frame 0' is oriented such that the z-axis points along joint 1 and the y-axis points to the apex of the sphere. The link angle,  $\alpha_{i+1}$  expresses the angle between the  $i$ th and  $(i + 1)$ th axis defined by the mechanism geometry. The rotation angle  $\theta_i$  defines the variable joint angle as a between the rotation axis  $i - 1$  and axis  $i$ .

For the parallel mechanism, when  $\theta_1 = 0$  and  $\theta_2 = 0$ , Link13 and Link24 lie in planes perpendicular to the plane created by intersecting axes  $z_1$  and  $z_2$ . There are two possible solutions to the orientations of Link35 and Link46 such that the mechanism is closed. The default orientation will be the orientation for which

$\theta_6 < 180^\circ$ . This will be referred to as the ‘end-effector in’ orientation. For the serial mechanism, when  $\theta_1 = 0$  Link13 lies in a plane perpendicular to the plane created by intersecting axes  $z1$  and  $x1$ . When  $\theta_3 = 0$ , Link35 is folded back onto  $L_{13}$ .

The transformation matrices between frames (8.1) are based on the DH-parameter notation that is summarized in Table 8.1. Because all the joints’ translation parameters ( $a_i$ ,  $d_i$ ) are zero, the kinematic problem is reduced to describing the orientation of the end-effector in space. Thus, the generalized frame transformation matrix is reduced from the typical  $4 \times 4$  translation and rotation matrix, to a  $3 \times 3$  rotation matrix (8.1). The short notation for trigonometric functions  $\sin$  and  $\cos$  as  $c$  and  $s$  will be used throughout the manuscript.

$${}^{i-1}R = \begin{bmatrix} c\theta_i & -s\theta_i & 0 \\ s\theta_i c\alpha_{i-1} & c\theta_i c\alpha_{i-1} & -s\alpha_{i-1} \\ s\theta_i s\alpha_{i-1} & c\theta_i s\alpha_{i-1} & c\alpha_{i-1} \end{bmatrix} \quad (8.1)$$

### 8.2.2.2 Forward Kinematics

Given the mechanism parameters ( $\alpha_{i-1}$ ,  $\theta_i$ ) the forward kinematics defines the orientation of the end-effector  ${}^o'u$  expressed in Frame  $O'$ . The following sections describe the forward kinematics of the parallel and serial mechanisms.

#### Parallel Manipulator

Given the two joint angles  $\theta_1$  and  $\theta_2$ , to find the end-effector orientation the full pose of the mechanism must first be solved. A geometric or analytical approach may be utilized in order to solve for parallel mechanism joint angles  $\theta_3$ ,  $\theta_4$  and  $\theta_5$ .

The first step in the geometric solution is posing Link13 and Link24 based on joint rotation angles  $\theta_1$  and  $\theta_2$ . The second step is to sweep links Link35 and Link46 through their range of motion by varying the joint angles  $\theta_3$  and  $\theta_4$ . A closed chain parallel manipulator is formed at the intersection of the two paths swept by joints 5 and 6.

The analytical approach was used, which involves taking a closed-loop coordinate transformation around the 5R parallel manipulator, starting and ending at the same frame (Frame 1). The rotation matrix around a closed chain is equal to an identity matrix  $I$  formed as a series of transformation matrices. Using the rotation matrices  ${}^{i-1}R$  around the closed chain and the specified joint angles  $\theta_1$  and  $\theta_2$  (8.2) sets up a system of three equations and three unknown joint angles,  $\theta_3$ ,  $\theta_4$  and  $\theta_6$ .

$$I = {}^1R = {}^1R_3 {}^3R_5 {}^5R_6 {}^6R_4 {}^4R_2 {}^2R_0 {}^0R_{0'} {}^0R_1 {}^0'R_1 \quad (8.2)$$

The resultant matrix equation is given in terms of  $\sin\theta_i$  and  $\cos\theta_i$  ( $i = 3, 4, 6$ ) In order to solve for the two solutions of this system the following trigonometric relation is needed

$$s\theta_i = \pm\sqrt{1 - c^2\theta_i} \quad (8.3)$$

Once all the joints angles ( $\theta_1 \dots \theta_6$ ) are known, the end-effector orientation can be determined by utilizing the forward kinematics expression of one serial manipulator subset. See the following section for details.

### Serial Manipulator

Given the two joint angles  $\theta_1$  and  $\theta_3$ , the forward kinematics of the 2R serial mechanism define the orientation of the end-effector. Using the rotation matrices ( ${}^{i-1}_iR$ ) – (1) and the joint parameters (Table 8.1), the coordinate transformation from the base to the end-effector is expressed as

$${}^0_5R = {}^0_1R {}^1_3R {}^3_5R \quad (8.4)$$

One may note that tool roll,  $\theta_5$ , is not represented in (4). As a result, rather than expressing the entire orientation of the end-effector frame, it is sensible to express a vector that is collinear with the end-effector axis,  $Z_5$ . This vector is expressed in Frame 5 as  ${}^5u_z = [0 \ 0 \ 1]^T$ . The end-effector axis,  $Z_5$  vector in Frame  $O'$  ( ${}^{O'}u$ ) is given by (5) using (4). The vector  ${}^{O'}u$  has its origin at the center of the sphere, and it points along the mechanism's end-effector, representing the orientation of the tool attached to the end-effector.

$${}^{O'}u = \begin{bmatrix} {}^{O'}u_x \\ {}^{O'}u_y \\ {}^{O'}u_z \end{bmatrix} = {}^0_5R \begin{bmatrix} 0 \\ 0 \\ 1 \end{bmatrix} = \begin{bmatrix} c\theta_1 s\theta_3 s\alpha_{35} + s\theta_1 c\theta_3 c\alpha_{13} - s\theta_1 s\alpha_{13} c\alpha_{35} \\ s\theta_1 s\theta_3 s\alpha_{35} - c\theta_1 c\theta_3 c\alpha_{13} - c\theta_1 s\alpha_{13} c\alpha_{35} \\ c\theta_3 s\alpha_{13} s\alpha_{35} + c\alpha_{13} c\alpha_{35} \end{bmatrix} \quad (8.5)$$

#### 8.2.2.3 Inverse Kinematics

Given the mechanism parameters ( $\alpha_{i-1}$ ) and the end-effector orientation  ${}^{O'}u$  expressed in Frame  $O'$  the inverse kinematics defines the mechanism joint angles ( $\theta_i$ ). Multiple solutions are available for any  ${}^{O'}u$  in the workspace for both parallel and serial mechanism configurations. However, due to practical considerations of the physical joint limits, all the solutions are eliminated except one.

### Parallel Manipulator

For any  ${}^0u$ , the inverse kinematics result in four different solutions. The “elbow up/down” combinations of the two serial arms correspond to the four solutions that define the unique poses of the mechanism.

Using the Z component  ${}^0u_z$  (the third line of  ${}^0u_z - (5)$ ) results in

$$c\theta_3 = \frac{{}^0u_z - c\alpha_{13} c\alpha_{35}}{s\alpha_{13} s\alpha_{35}} \quad (8.6)$$

The two solutions for  $\theta_3$  are as follows:

$$\theta_{3a}, \theta_{3b} = a \tan 2 \left( \pm \sqrt{1 - c^2\theta_3}, c\theta_3 \right) \quad (8.7)$$

Using the expression for  ${}^0u_x, {}^0u_y$  (the first and second lines of  ${}^0u - (5)$ ) and the previous result, then solving for  $\sin\theta_1$  and  $\cos\theta_1$ , results in (8).

$$c\theta_1 = \frac{{}^0u_x s\theta_3 s\alpha_{35} - {}^0u_y (c\theta_3 c\alpha_{13} s\alpha_{35} - s\alpha_{13} c\alpha_{35})}{(s\theta_3 s\alpha_{35})^2 + (c\theta_3 c\alpha_{13} s\alpha_{35} - s\alpha_{13} c\alpha_{35})^2}$$

$$s\theta_1 = \frac{{}^0u_y s\theta_3 s\alpha_{35} + {}^0u_x (c\theta_3 c\alpha_{13} s\alpha_{35} - s\alpha_{13} c\alpha_{35})}{(s\theta_3 s\alpha_{35})^2 + (c\theta_3 c\alpha_{13} s\alpha_{35} - s\alpha_{13} c\alpha_{35})^2} \quad (8.8)$$

$$\theta_1 = \text{atan2}(s\theta_1, c\theta_1)$$

Thus, the inverse kinematic equations provide two solutions to the pose of the odd side of the manipulator,  $\theta_{1a}$  and  $\theta_{3a}$ , and  $\theta_{1b}$  and  $\theta_{3b}$ .

The even side of the manipulator is solved in a similar fashion. The end-effector z-axis in Frame 5 vector expressed in Frame  $O'$  ( ${}^0'u$ ) is first translated into Frame  $O''$ .

$${}^0''u = {}^0'R {}^0'u \quad (8.9)$$

$$c\theta_4 = \frac{{}^0''u_z - c\alpha_{24} c\alpha_{46}}{s\alpha_{24} s\alpha_{46}} \quad (8.10)$$

$$\theta_{4a}, \theta_{4b} = \text{atan2} \left( \pm \sqrt{1 - c^2\theta_4}, c\theta_4 \right) \quad (8.11)$$

$$c\theta_2 = \frac{{}^0''u_x s\theta_4 s\alpha_{46} - {}^0''u_y (c\theta_4 c\alpha_{24} s\alpha_{46} - s\alpha_{24} c\alpha_{46})}{(s\theta_4 s\alpha_{46})^2 + (c\theta_4 c\alpha_{24} s\alpha_{46} - s\alpha_{24} c\alpha_{46})^2}$$

$$s\theta_2 = \frac{{}^0''u_y s\theta_4 s\alpha_{46} + {}^0''u_x (c\theta_4 c\alpha_{24} s\alpha_{46} - s\alpha_{24} c\alpha_{46})}{(s\theta_4 s\alpha_{46})^2 + (c\theta_4 c\alpha_{24} s\alpha_{46} - s\alpha_{24} c\alpha_{46})^2} \quad (8.12)$$

$$\theta_2 = \text{atan2}(s\theta_2, c\theta_2)$$



**Table 8.2** Parallel and serial manipulator D–H parameters. The serial manipulator represents a subset of the parallel manipulator denoted by the even link number. Its D–H parameters are marked by a gray background (see Fig. 8.3 for details)

$i - 1$	$i$	$I + 1$	$\alpha_{i-1}$	$\theta_i$
0'	1	3	0	$\theta_1$
1	3	5	$-\alpha_{13}$	$\theta_3$
3	5	–	$\alpha_{35}$	$\theta_5 = 0$
0''	0''	2	$\alpha_{12}$	0
0''	2	4	0	$\theta_2$
2	4	6	$-\alpha_{24}$	$\theta_4$
4	6	5	$\alpha_{46}$	$\theta_6$

**Table 8.3** Four solutions to the inverse kinematic problem for parallel manipulator (Two solutions to the inverse kinematic problem for serial manipulator are shaded in gray)

Pose 1	$\theta_{1a}$	$\theta_{3a}$	$\theta_{2a}$	$\theta_{4a}$
Pose 2	$\theta_{1a}$	$\theta_{3a}$	$\theta_{2b}$	$\theta_{4b}$
Pose 3	$\theta_{1b}$	$\theta_{3b}$	$\theta_{2a}$	$\theta_{4a}$
Pose 4	$\theta_{1b}$	$\theta_{3b}$	$\theta_{2b}$	$\theta_{4b}$

Providing two solutions to the pose of the even side of the manipulator,  $\theta_{2a}$  and  $\theta_{4a}$ , and  $\theta_{2b}$  and  $\theta_{4b}$ . The complete solution of the inverse kinematic problem for all four configurations is summarized in Table 8.3.

### Serial Manipulator

The serial mechanism may be considered as a subset of the parallel mechanism, and therefore the inverse kinematics of the odd side of the parallel mechanism is the solution to the inverse kinematics of the serial mechanism. The two solutions to the inverse kinematics problem for the serial manipulator are summarized in Table 8.2 highlighted in gray.

#### 8.2.2.4 Jacobian Matrix

The Jacobian matrix  ${}^A J$ , the mapping between joint velocities ( $\dot{\theta}_i$ ) and end-effector angular velocities ( ${}^i \omega_5$ ), can be expressed with respect to any frame ( $A$ ) associated with the mechanism. The advantage of expressing the Jacobian matrix in the end-effector frame (Frame 5) – ( ${}^5 J$ ) is that the last row of the matrix is  $[0 \ 0 \ 1]$  for all poses and joint velocities. Therefore, for computational purposes, the Jacobian matrix ( ${}^5 J$ ) may be reduced by one dimension using only the upper  $2 \times 2$  submatrix of the full  $3 \times 3$  Jacobian. This truncated version of the Jacobian maps the two controlled joint velocities ( $\dot{\theta}_1, \dot{\theta}_2$  of the parallel mechanism and  $\dot{\theta}_1, \dot{\theta}_3$  of the serial

mechanism) to end-effector angular velocity. This version of the Jacobian will later be used for calculating the manipulator isotropy.

### Parallel Manipulator

The Jacobian matrix of the parallel mechanism, expressed in Frame 5 ( ${}^5J_{par}$ ) is a  $3 \times 3$  matrix mapping the input joint velocities ( $\dot{\theta}_1, \dot{\theta}_2, \dot{\theta}_5$ ) to the end-effector angular velocities ( ${}^5\omega_5$ , (12)). The method we used for obtaining the Jacobian matrix is to develop its inverse form using  ${}^5J_{serial}$  for the even and odd sides. From these we can construct  ${}^5J_{par}^{-1}$  and then invert this expression.

$$\begin{bmatrix} {}^5\omega_{5x} \\ {}^5\omega_{5y} \\ {}^5\omega_{5z} \end{bmatrix} = [{}^5J_{Par}]_{3 \times 3} \begin{bmatrix} \dot{\theta}_1 \\ \dot{\theta}_2 \\ \dot{\theta}_5 \end{bmatrix} \quad (8.13)$$

As previously explained the upper  $2 \times 2$  submatrix of the Jacobian matrix  ${}^5J_{par}$  maps the two input joint velocities ( $\dot{\theta}_1, \dot{\theta}_2$ ) to the end-effector angular velocities ( ${}^5\omega_5$ ) of pitch and yaw. Eliminating tool roll,

$$\begin{bmatrix} {}^5\omega_{5x} \\ {}^5\omega_{5y} \end{bmatrix} = [{}^5J_{par}]_{2 \times 2} \begin{bmatrix} \dot{\theta}_1 \\ \dot{\theta}_2 \end{bmatrix} \quad (8.14)$$

We used a standard recursive formulation of link  $i + 1$  angular velocity expressed in frame  $i + 1$  ( ${}^{i+1}\omega_{i+1}$ ) to derive the Jacobian matrices of the odd and even numbered arms, treated as independent serial manipulators  ${}^5J_{SerialOdd}$  and  ${}^5J_{SerialEven}$ . Note that by definition, joint  $i + 1$  is always rotated along its Z axis denoted by a unit vector  $\hat{z}_{i+1}$ . Using recursive (15) and tracing the odd arm and even arms of the mechanism from Frame 5 to the base frame results in (16) and (17).

$${}^{i+1}\omega_{i+1} = {}_i^{i+1}R^i \omega_i + \dot{\theta}_{i+1}^{i+1} \hat{z}_{i+1} \quad (8.15)$$

$${}^5\omega_5 = {}_1^5R \begin{bmatrix} 0 \\ 0 \\ 1 \end{bmatrix} \dot{\theta}_1 + {}_3^5R \begin{bmatrix} 0 \\ 0 \\ 1 \end{bmatrix} \dot{\theta}_3 + \begin{bmatrix} 0 \\ 0 \\ 1 \end{bmatrix} \dot{\theta}_5 \quad (8.16)$$

$${}^5\omega_5 = {}_2^5R \begin{bmatrix} 0 \\ 0 \\ 1 \end{bmatrix} \dot{\theta}_2 + {}_4^5R \begin{bmatrix} 0 \\ 0 \\ 1 \end{bmatrix} \dot{\theta}_4 + \begin{bmatrix} 0 \\ 0 \\ 1 \end{bmatrix} (\dot{\theta}_5 + \dot{\theta}_6) \quad (8.17)$$

which is simplified into (18) and (19) to get the Jacobian matrix of the odd and even numbered sides

$$\begin{aligned}
\begin{bmatrix} {}^5\omega_{5x} \\ {}^5\omega_{5y} \\ {}^5\omega_{5z} \end{bmatrix} &= [{}^5J_{SerialOdd}] \begin{bmatrix} \dot{\theta}_1 \\ \dot{\theta}_3 \\ \dot{\theta}_5 \end{bmatrix} \\
&= \begin{bmatrix} [{}^5_1R] \begin{bmatrix} 0 \\ 0 \\ 1 \end{bmatrix} & [{}^5_3R] \begin{bmatrix} 0 \\ 0 \\ 1 \end{bmatrix} & \begin{bmatrix} 0 \\ 0 \\ 1 \end{bmatrix} \end{bmatrix} \begin{bmatrix} \dot{\theta}_1 \\ \dot{\theta}_3 \\ \dot{\theta}_5 \end{bmatrix}
\end{aligned} \tag{8.18}$$

$$\begin{aligned}
\begin{bmatrix} {}^5\omega_{5x} \\ {}^5\omega_{5y} \\ {}^5\omega_{5z} \end{bmatrix} &= [{}^5J_{SerialEven}] \begin{bmatrix} \dot{\theta}_2 \\ \dot{\theta}_4 \\ \dot{\theta}_5 + \dot{\theta}_6 \end{bmatrix} \\
&= \begin{bmatrix} [{}^5_2R] \begin{bmatrix} 0 \\ 0 \\ 1 \end{bmatrix} & [{}^5_4R] \begin{bmatrix} 0 \\ 0 \\ 1 \end{bmatrix} & \begin{bmatrix} 0 \\ 0 \\ 1 \end{bmatrix} \end{bmatrix} \begin{bmatrix} \dot{\theta}_2 \\ \dot{\theta}_4 \\ \dot{\theta}_5 + \dot{\theta}_6 \end{bmatrix}
\end{aligned} \tag{8.19}$$

By inverting these equations we obtain

$$\begin{aligned}
\begin{bmatrix} \dot{\theta}_1 \\ \dot{\theta}_3 \\ \dot{\theta}_5 \end{bmatrix} &= \begin{bmatrix} [{}^5_1R] \begin{bmatrix} 0 \\ 0 \\ 1 \end{bmatrix} & [{}^5_3R] \begin{bmatrix} 0 \\ 0 \\ 1 \end{bmatrix} & \begin{bmatrix} 0 \\ 0 \\ 1 \end{bmatrix} \end{bmatrix}^{-1} \begin{bmatrix} {}^5\omega_{5x} \\ {}^5\omega_{5y} \\ {}^5\omega_{5z} \end{bmatrix} \\
&= [{}^5J_{SerialOdd}]^{-1} \begin{bmatrix} {}^5\omega_{5x} \\ {}^5\omega_{5y} \\ {}^5\omega_{5z} \end{bmatrix}
\end{aligned} \tag{8.20}$$

$$\begin{aligned}
\begin{bmatrix} \dot{\theta}_2 \\ \dot{\theta}_4 \\ \dot{\theta}_5 + \dot{\theta}_6 \end{bmatrix} &= \begin{bmatrix} [{}^5_2R] \begin{bmatrix} 0 \\ 0 \\ 1 \end{bmatrix} & [{}^5_4R] \begin{bmatrix} 0 \\ 0 \\ 1 \end{bmatrix} & \begin{bmatrix} 0 \\ 0 \\ 1 \end{bmatrix} \end{bmatrix}^{-1} \begin{bmatrix} {}^5\omega_{5x} \\ {}^5\omega_{5y} \\ {}^5\omega_{5z} \end{bmatrix} \\
&= [{}^5J_{SerialEven}]^{-1} \begin{bmatrix} {}^5\omega_{5x} \\ {}^5\omega_{5y} \\ {}^5\omega_{5z} \end{bmatrix}
\end{aligned} \tag{8.21}$$

The first rows of (20) and (21) define  $\dot{\theta}^1$  and  $\dot{\theta}^2$  respectively as a function of end-effector angular velocity  ${}^5\omega_5$  and the inverted<sup>2</sup> Jacobian matrices of the even and odd arms respectively. For  $k = 1, 2, 3$ , the  $k$ th column of the Jacobian

$$\dot{\theta}^1 = [{}^5J_{SerialOdd}^{-1}(1, k)] [{}^5\omega_{5x} \quad {}^5\omega_{5y} \quad {}^5\omega_{5z}]^T \tag{8.22}$$

$$\dot{\theta}^2 = [{}^5J_{SerialEven}^{-1}(1, k)] [{}^5\omega_{5x} \quad {}^5\omega_{5y} \quad {}^5\omega_{5z}]^T \tag{8.23}$$

As previously explained, the benefit of expressing the Jacobian matrix in the end-effector Frame 5 is the following simple representation of the joint angular velocity.

$$\begin{bmatrix} \dot{\theta} \\ \dot{\theta} \\ \dot{\theta} \\ \dot{\theta} \\ \dot{\theta} \end{bmatrix}_5 = [0 \quad 0 \quad 1] \begin{bmatrix} {}^5\omega_{5x} & {}^5\omega_{5y} & {}^5\omega_{5z} \end{bmatrix}^T \quad (8.24)$$

Assembling individual joint velocities into matrix form allows us to formulate the inverse Jacobian for the parallel manipulator

$$\begin{bmatrix} \dot{\theta} \\ \dot{\theta} \\ \dot{\theta} \\ \dot{\theta} \\ \dot{\theta} \end{bmatrix} = \begin{bmatrix} {}^5J_{SerialOdd}^{-1}(1, k) & 0 \\ {}^5J_{SerialEven}^{-1}(1, k) & 0 \\ 0 & 0 & 1 \end{bmatrix} \begin{bmatrix} {}^5\omega_{5x} \\ {}^5\omega_{5y} \\ {}^5\omega_{5z} \end{bmatrix} \quad (8.25)$$

The relationship between the two input joint angular velocities ( $\dot{\theta}_1$  and  $\dot{\theta}_2$ ) and the angular velocity of the end-effector, considering only the pitch and yaw of the tool ( ${}^5\omega_{5x}$ ,  ${}^5\omega_{5y}$ ) allows us to analyze only the upper  $2 \times 2$  sub-matrix of the Jacobian Inverse. For  $k = 1, 2$

$$\begin{bmatrix} \dot{\theta} \\ \dot{\theta} \\ \dot{\theta} \\ \dot{\theta} \end{bmatrix} = \begin{bmatrix} {}^5J_{SerialOdd}^{-1}(1, k) \\ {}^5J_{SerialEven}^{-1}(1, k) \end{bmatrix} \begin{bmatrix} {}^5\omega_{5x} \\ {}^5\omega_{5y} \end{bmatrix} \quad (8.26)$$

Inverting this inverse Jacobian gives the Jacobian matrix for the parallel mechanism (14).

### Serial Manipulator

Using the odd numbered side of the parallel mechanism, the Jacobian matrix of the serial mechanism can be derived from (18). Based on the previous justification, the upper  $2 \times 2$  submatrix of the full  $3 \times 3$  Jacobian relates the controlled axes of motion to the end-effector velocity:

$$\begin{bmatrix} {}^5\omega_{5x} \\ {}^5\omega_{5y} \end{bmatrix} = [J_{5truncated}]_{2 \times 2} \begin{bmatrix} \dot{\theta}_1 \\ \dot{\theta}_3 \end{bmatrix} \quad (8.27)$$

### 8.2.3 Kinematic Optimization

Experimental results led to the definition of engineering requirements as derivatives from the clinical requirements (see Sect. 8.2.1). The optimization process was developed to define the mechanism parameters (link angles  $\alpha_{13}$ ,  $\alpha_{35}$ ,  $\alpha_{24}$ ,  $\alpha_{46}$ ,  $\alpha_{12}$ ) so that the workspace of the mechanism covers the entire EDWS while

providing high dexterity manipulation within the DWS. The goal of a high performance yet compact mechanism was achieved by careful selection of the scoring criteria.

Up to this point, the analysis has been purely mathematical. The manipulator could move through singularities, fold on itself and solve for arbitrary poses without regard to how a physically implemented device might accomplish this. Based on mechanical design of the serial manipulator the range of motion of the first joint angle is  $180^\circ$  ( $0^\circ < \theta_1 < 180^\circ$ ) and the range of motion of the second joint is  $160^\circ$  ( $20^\circ < \theta_3 < 180^\circ$ ). By adding these joint limits into the optimization, the true reachable workspace of a physically implemented device could be analyzed.

### 8.2.3.1 Mechanism Isotropy

The Jacobian matrix allows one to analyze the kinematic performance of a mechanism. One performance metric using the Jacobian matrix is Yoshiakawa's manipulability measure, specified in [20]. The manipulability measure most commonly used ranges from 1 to infinity.

$$\omega = \sqrt{\det(J(\theta)J^T(\theta))} \quad (8.28)$$

In contrast, mechanism isotropy is a scoring criterion that ranges from 0 to 1. Isotropy is defined in (29) as the ratio between the lowest eigenvalue ( $\lambda_{\min}$ ) and the highest eigenvalue ( $\lambda_{\max}$ ) of the Jacobian [37]. Note that the isotropy is a function of the mechanism's input joint angles ( $\theta_i$ ). For the serial mechanism, these angles are  $\theta_1, \theta_3$  and for the parallel mechanism,  $\theta_1, \theta_2$

$$ISO(\theta_i) = \frac{\lambda_{\min}}{\lambda_{\max}} \quad ISO \in \langle 0, 1 \rangle \quad (8.29)$$

Our analysis uses isotropy as the measure of performance because numerically the range of scores was easier to deal with. Given a design candidate (serial mechanism link angles  $\alpha_{13}$  and  $\alpha_{35}$  or parallel mechanism link angles  $\alpha_{13}, \alpha_{35}, \alpha_{24}, \alpha_{46}, \alpha_{12}$ ), for every mechanism pose there is an associated isotropy value in the range of 0–1. An isotropy measure of 0 means the mechanism is in a singular configuration and has lost a degree of freedom so there is a direction in which it can no longer move. An isotropy measure of 1 means the mechanism can move equally well in all directions.

Once the kinematic equations and a performance measure are defined, one can evaluate the performance of a particular design candidate at each point its workspace. The integration of the isotropy score over the DWS or EDWS is used as one component of a scoring function for the specific design candidate.

### 8.2.3.2 Scoring Criteria and Cost Function

Each design candidate must be assigned a single score so that the best overall manipulator design can be selected. Three individual criteria including (1) an integrated average score (2) a minimal single score (3) the cube of the angular link length are incorporated into the composite score, expressed in (31).

In order to analyze the mechanism, the hemisphere was discretized into points distributed equally in azimuth and elevation. Each point is associated with a different area of the hemisphere based on elevation angle. One measure of how well a manipulator performs is to calculate the isotropy at each point, multiply by its corresponding area, then sum all of the weighed point-scores over the the DWS or EDWS. This provides an average performance of the design candidate over the workspace.

The set ( $K$ ) of all possible cones ( $k$ ) on the hemisphere with an azimuth angle ( $\sigma$ ) and elevation angle ( $\zeta$ ) is

$$K = \{k(\sigma, \zeta) : 0 < \sigma < 2\pi, 0 < \zeta < \pi/4\} \quad (8.30)$$

The set of discrete points ( $k_{\sigma, \zeta}^p$ ) contained in the cone ( $k_{\sigma, \zeta}$ ) is

$$k_{\sigma, \zeta}^p \subset k_{\sigma, \zeta} \quad (8.31)$$

Each point has an associated isotropy and area. Thus the scoring functions are

$$S_{sum} = MAX_K \left\{ \sum_{k_{\sigma, \zeta}^p} ISO(\theta_1, \theta_3) * Area(\sigma, \zeta) \right\} \quad (8.32a)$$

$$S_{min} = MAX_K \left\{ MIN_{k_{\sigma, \zeta}^p} (ISO(\theta_1, \theta_3)) \right\} \quad (8.32b)$$

There are many orientations of the DWS or EDWS with respect to the hemisphere, noted as the set  $K$ . Each design candidate has a  $S_{sum}$  value that corresponds to the highest summed isotropy score for that design.

The limitation of a summed isotropy score is that singularities or workspace boundaries could exist within a region that has a good summed score. The minimum isotropy value within the cone intersection area is an indicator of the worst performance that can be expected over that area. For each design candidate the highest minimum isotropy score on the set of all cones,  $K$ , will be referred to as  $S_{min}$ .

While a dynamic analysis is not explicitly addressed in this study, there is a relationship between mass and size of a robot with dynamic performance. A design with greater link angles will have a larger reachable workspace and generally better

$S_{sum}$  and  $S_{min}$  values. The drawback to larger link angles is reduced link stiffness and higher mass and inertia (worse dynamic performance) compared to shorter links. Based on long beam theory the mechanism stiffness is inversely proportional to the cube of the sum of the link length (expressed as angles in the spherical case) [28]. As suggested by the experimental findings, in surgery the mechanism needs to be operated in the smallest possible workspace that will satisfy the motion requirements of the surgical tool. Thus, the optimization goal is to maximize the kinematic performance over the surgical workspace while minimizing the link length.

Our composite design candidate performance function takes into account all three individual criteria and is defined as follows

$$\phi = \frac{S_{sum} \cdot S_{min}}{(\alpha_{13} + \alpha_{35})^3} \quad (8.33)$$

A requirement of the optimization is that over the target workspace, the mechanism does not encounter any singularities or workspace boundaries. By multiplying the summed isotropy by the minimum isotropy, candidates that fail to meet the requirement have a score of zero. By dividing by the cube of the sum of the link angles, the score penalizes mechanism compliance and inertia. Thus, in a scan of the potential design space, the peak composite score should represent a design with maximum average performance, a guaranteed minimum performance and good mechanical properties.

### 8.2.3.3 Optimization Algorithm

Considering the target workspace to be the DWS, the 60° cone's orientation in azimuth and elevation was varied in order to obtain the best orientation of the DWS for that design candidate. Optimizing for the EDWS, which is an elliptical cone, would add another design parameter, namely cone roll angle. Introducing an additional parameter will increase execution time of the optimization by an order of magnitude. By considering the target workspace to be a 90° cone that encompasses all roll angle orientations of the EDWS, an additional design parameter is avoided. This 90° cone will further be referred to as a superset of the EDWS. Using a superset of the EDWS could result in larger links than necessary; a design that can reach 60° in one direction and 90° in an orthogonal direction may satisfy the EDWS cone but not the superset 90° cone.

The algorithm for evaluating a design candidate is as follows: (1) Define a hemisphere with points distributed evenly in azimuth and elevation (2) Calculate inverse kinematics and isotropy for each point (3) Define a target cone (DWS or superset of the EDWS) (a) Move cone around the hemisphere (b) At each orientation of target cone, calculate integrated isotropy and minimum isotropy within the cone (4) Save the best minimum and integrated scores for that design candidate

## Parallel Manipulator

The parallel manipulator is composed of five links. The optimization considered a symmetric device therefore taking into account three mechanism parameters; Base Angle ( $\alpha_{12}$ ), Link1 ( $\alpha_{13} = \alpha_{24}$ ) and Link2 ( $\alpha_{35} = \alpha_{46}$ ). Link1 and Link2 were varied from  $32^\circ$  to  $90^\circ$  in  $2^\circ$  increments and  $\alpha_{12}$  from  $0^\circ$  to  $90^\circ$  in  $2^\circ$  increments for a total of 40,500 design candidates. The hemisphere was discretized into 900 points, distributed evenly in azimuth and elevation angles. The optimization can be summarized:

$$\max \phi (\alpha_{12}, \text{Link1}, \text{Link2}) \quad \left\{ \begin{array}{l} 0^\circ < \alpha_{12} < 90^\circ \\ 32^\circ < \text{Link1} < 90^\circ \\ 32^\circ < \text{Link2} < 90^\circ \end{array} \right. \quad (8.34)$$

The composite score,  $\phi$ , of the parallel mechanism as a function of the link length angles Link1 ( $\alpha_{13} = \alpha_{24}$ ), Link2 ( $\alpha_{35} = \alpha_{46}$ ) and a base link length of  $\alpha_{12} = 0$  is plotted in Fig. 8.4 with a target workspace, the DWS (Fig. 8.5a) and the EDWS superset (Fig. 8.5b). These plots of Link1 and Link2 versus score for a fixed base angle will be referred to as ‘optimization design subspace plots’. Searching through the entire design space, optimizing on the DWS indicates a peak composite score of 0.1319 was achieved by a parallel manipulator with link angles  $\alpha_{13} = \alpha_{24} = 38^\circ$  (Link 1) and  $\alpha_{35} = \alpha_{46} = 50^\circ$  (Link 2) and base angle  $0^\circ$ . In contrast, running the same optimization but using the superset of the EDWS as the target workspace gave link angles  $\alpha_{13} = \alpha_{24} = 52^\circ$  (Link 1) and  $\alpha_{35} = \alpha_{46} = 72^\circ$  (Link 2) and base angle  $0^\circ$  with a score of 0.0960.

An important parameter for the parallel mechanism is the base angle,  $\alpha_{12}$ . A sequence of plots (Fig. 8.6) of the parallel mechanism composite score for different base angles  $\alpha_{12} = 90^\circ - 0^\circ$  shows the overall dependency between the mechanism’s best design in terms of link length and the base angle. This sequence of plots indicated that the performance of the parallel mechanism increased as the base angle decreased.

The maximal performance score as a function of the base angle is depicted in Fig. 8.5. This result indicates that the performance score decreases as the base angle increases in the range of  $0-70^\circ$  with a minimal value at a base angle equal to  $70^\circ$ . In the range of  $70-90^\circ$  a reversed behavior is observed in which the performance score increases as the base angle decreases.

In order to demonstrate how base angle,  $\alpha_{12}$ , effects the mechanism workspace, a mechanism with fixed link lengths was chosen ( $\alpha_{13} = \alpha_{24} = \alpha_{35} = \alpha_{46} = 60^\circ$ ) and the base angle was varied. The workspace of each design is plotted as a sequence of figures (Fig. 8.8). The gray region the reachable workspace and black is the unreachable or singular region with the area of highest isotropy in dark gray. With a  $0^\circ$  base angle, the region of highest isotropy is a large strip whereas for  $90^\circ$  and  $45^\circ$  base angles it is a point.



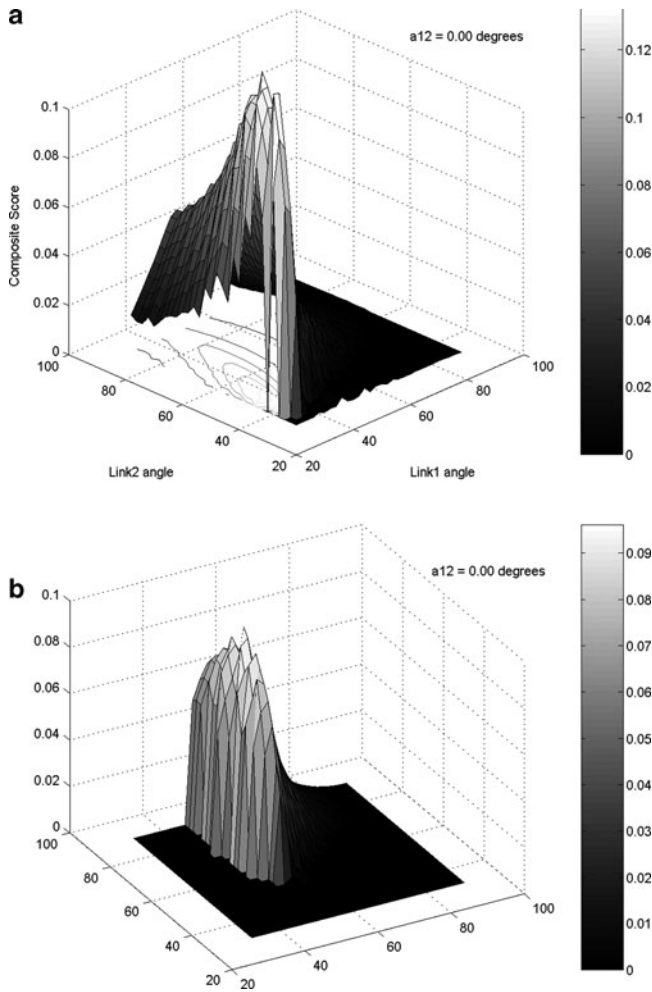


**Fig. 8.4** The Composite score  $\phi$  of the parallel mechanism as a function of the link lengths angles Link1 ( $\alpha_{13} = \alpha_{24}$ ), Link2 ( $\alpha_{35} = \alpha_{46}$ ) and a base link length of  $\alpha_{12} = 0$ : (a) Optimization design subspace plot with base angle  $0^\circ$  for DWS (b) Optimization design subspace plot with base angle  $0^\circ$  for EDWS superset

### Serial Manipulator

The Serial mechanism is composed of two links. The optimization considered all combinations of  $\alpha_{13}$  and  $\alpha_{35}$  from  $16^\circ$  to  $90^\circ$  in 2 increments for a total of 1,444 design candidates. The hemisphere was discretized into 3,600 points, distributed evenly in azimuth and elevation.

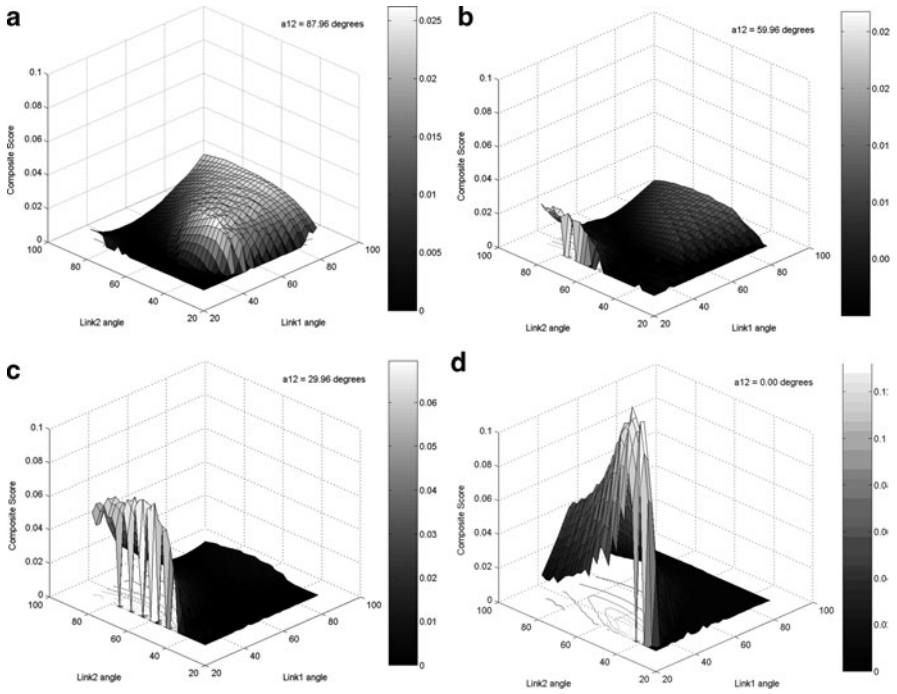


**Fig. 8.5** The composite score  $\phi$  of a parallel mechanism as a function of the link lengths angles Link 1 ( $\alpha_{13} = \alpha_{24}$ ) Link 2 ( $\alpha_{35} = \alpha_{45}$ ) with varying base angle  $\alpha_{12} = 90^\circ$  (a);  $60^\circ$  (b);  $30^\circ$  (c);  $0^\circ$  (d)

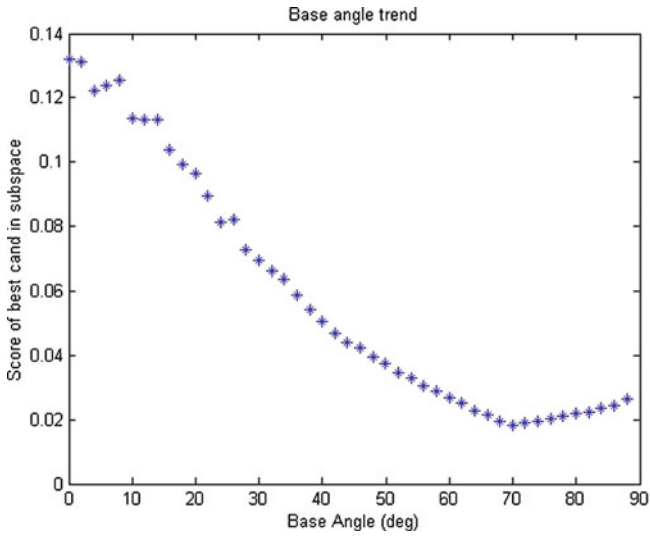


**Fig. 8.6** The composite score  $\varphi$  of a parallel mechanism as a function of the link lengths angles Link1 ( $\alpha_{13} = \alpha_{24}$ ), Link2 ( $\alpha_{35} = \alpha_{46}$ ) with varying base angle  $\alpha_{12} = 90$  (a);  $60$  (b);  $30$  (c)  $0$  (d)

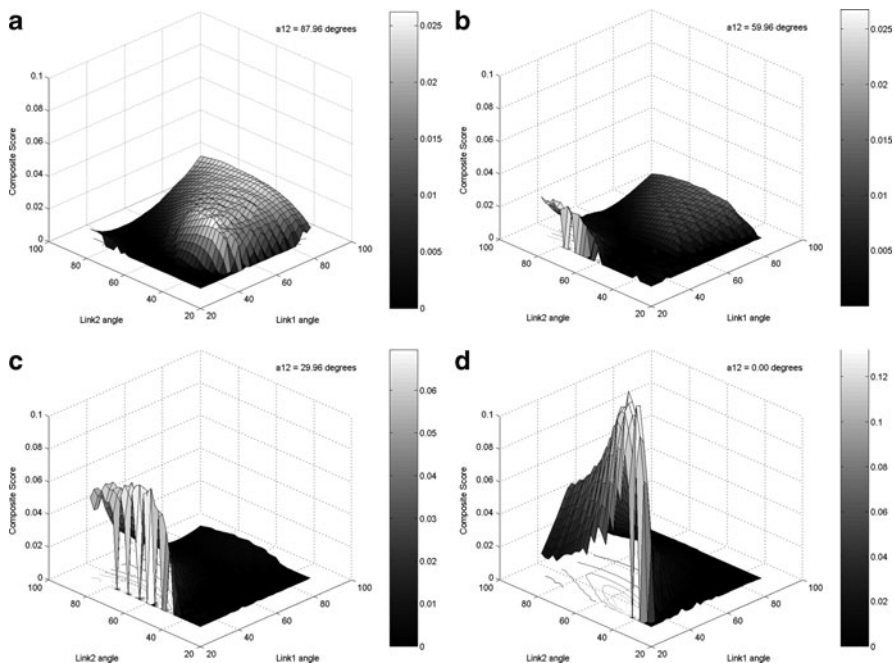


**Fig. 8.7** Parallel mechanism peak performance for a fixed link length as a function of the mechanism base angle

$$\max \phi (\alpha_{13}, \alpha_{35}) \begin{cases} 16^\circ < \alpha_{13} < 90^\circ \\ 16^\circ < \alpha_{35} < 90^\circ \end{cases} \quad (8.35)$$

Using the scoring criteria and hemisphere point resolution of  $2^\circ$ , a numerical scan of the serial mechanism design space was performed using all the combinations of link angles  $\alpha_{13}$  and  $\alpha_{35}$  in the range of  $16\text{--}90^\circ$ . For the serial manipulator optimized for the DWS, the best design was achieved with link angles of  $\alpha_{13} = 52^\circ$  (Link 1) and  $\alpha_{35} = 40^\circ$  (Link 2) and with a composite score of 0.0520 (Fig. 8.9a). In contrast, running the same optimization for the EDWS superset indicated that the optimal mechanism design has link angles  $\alpha_{13} = 90^\circ$  (Link 1) and  $\alpha_{35} = 72^\circ$  (Link 2) with a score of 0.0471 (Fig. 8.9b).

The difference in the results is not unexpected but it does pose an interesting dilemma. If one chooses the design that optimizes on a  $90^\circ$  cone, the resulting design might satisfy the requirements for a larger number of applications. However, this design has lower overall performance and larger links. A compromise between the requirements to maximize performance in the DWS and minimizing the size of the mechanism while being able to reach the EDWS was achieved by selecting the highest performing design over the DWS subject to the requirement that it also can reach the EDWS superset. Considering all the potential mechanism design candidates for the DWS (Fig. 8.9a) and eliminating those that cannot reach the EDWS

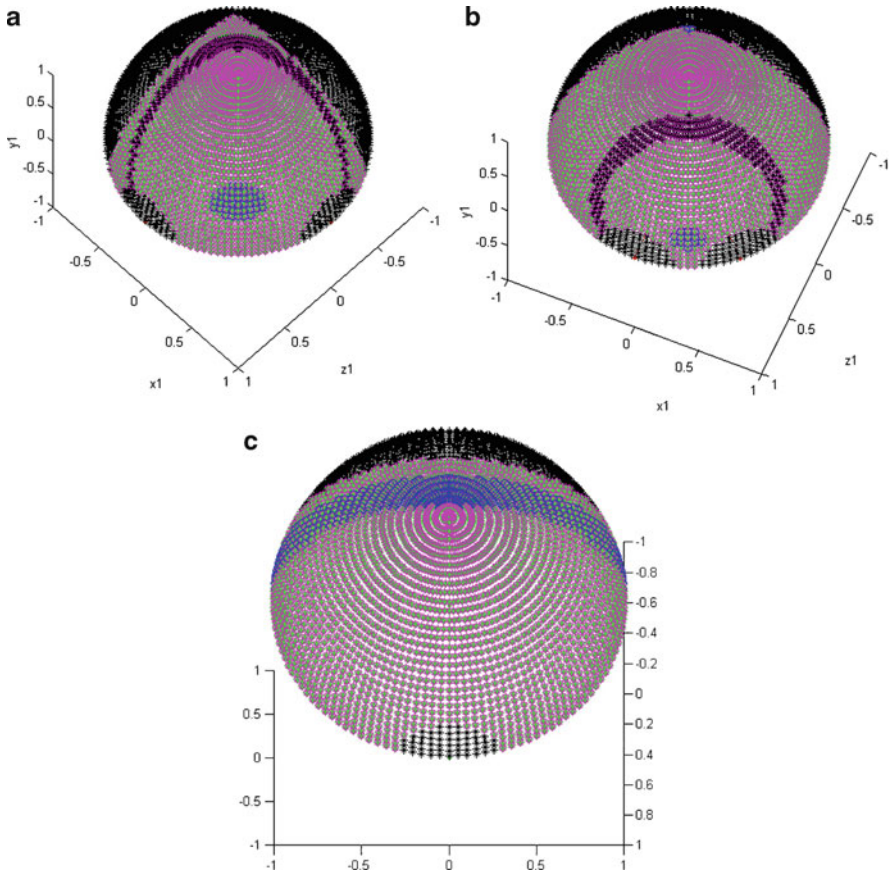


**Fig. 8.8** The parallel mechanism workspace link lengths:  $\alpha_{13} = \alpha_{24} = \alpha_{35} = \alpha_{46} = 60^\circ$  as a function of base angle  $\alpha_{12} = 90^\circ$ (a);  $45^\circ$ (b);  $0^\circ$ (c)

give the subset plotted in Fig. 8.9e. The highest performing design from this subset had link angles of  $\alpha_{13} = 74^\circ$  and  $\alpha_{35} = 60^\circ$  and a score of 0.0367.

### 8.3 System Architecture and Integration

The system includes two main sub systems: (1) the surgical console (master) and (2) the surgical robot (slave). To enable teleportation the master and the slave may be connected through various network layers for example wired, wireless, and hybrid communication links. Figure 8.10 provide an overview of the system architecture. The surgeon initiates the movement of the robot by moving the taylor of a haptic master input device. The position of the stylus is sensed by position sensors embedded in the master joints and acquired by the A/D converter that is

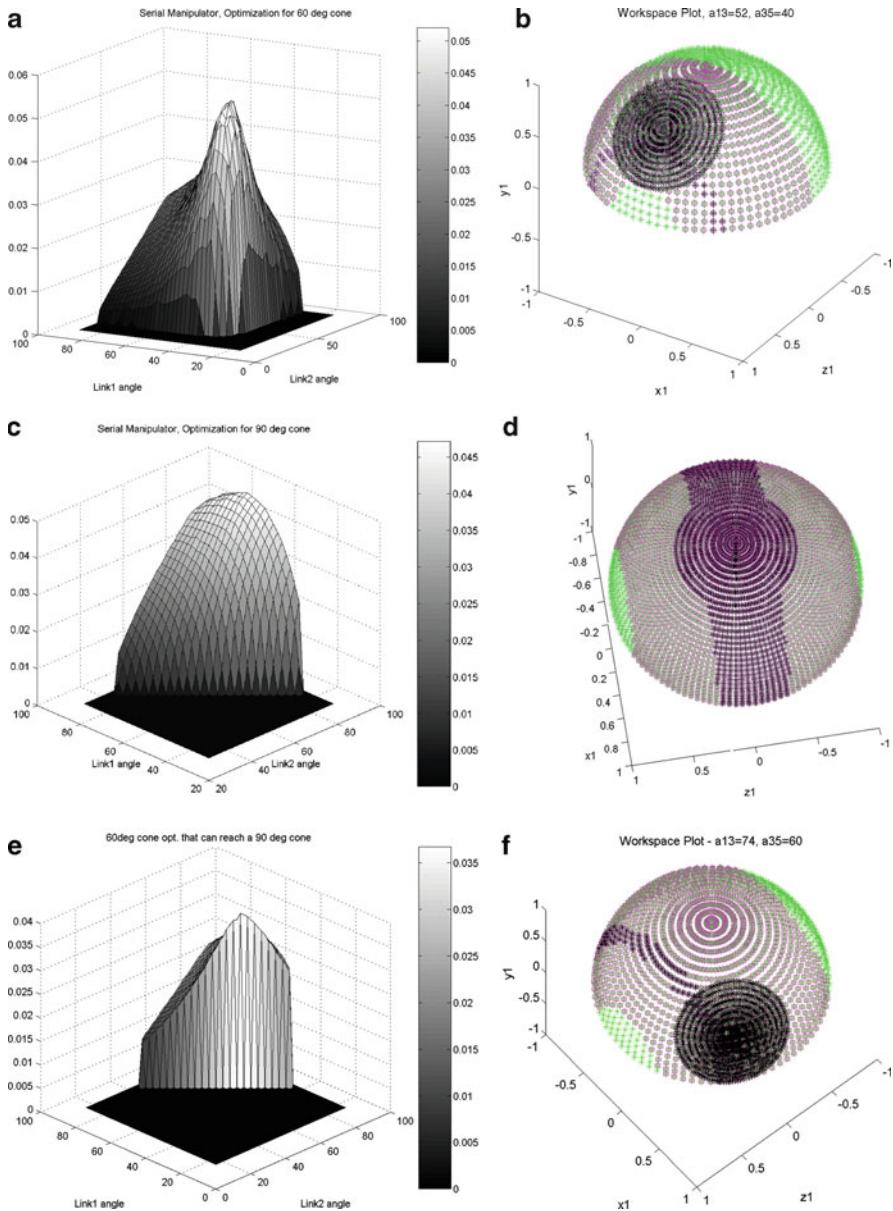


**Fig. 8.9** The composite score  $\varphi$  of a serial mechanism as a function of the link length angles Link1 ( $\alpha_{13} = \alpha_{24}$ ), Link2 ( $\alpha_{35} = \alpha_{46}$ ) along with the workspace of the mechanism with the best performance for each design criterion (peak of a) DWS, a cone with a vertex angle of  $60^\circ$  (b) Workspace plot for optimal mechanism (a) with link angles  $\alpha_{13} = 52^\circ$  and  $\alpha_{35} = 40^\circ$  (c) EDWS, a cone with a vertex angle of  $90^\circ$  (d) Workspace plot for optimal mechanism (peak of c) with link angles  $\alpha_{13} = 90^\circ$  and  $\alpha_{35} = 72^\circ$ , (e) subset of (a) which can reach a cone with a vertex angle of  $90^\circ$ . (f) Workspace plot for optimal mechanism (peak of e) with link angles  $\alpha_{13} = 74^\circ$  and  $\alpha_{35} = 60^\circ$ . For subplots c,d,f, the workspace plots show the hemisphere in green, the reachable workspace in purple, and the orientation of the best cone in black, with the strip of maximum isotropy also in black

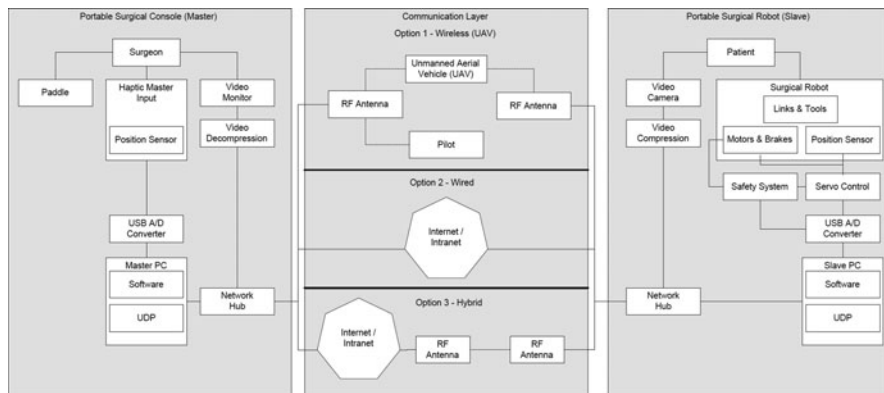


**Fig. 8.10** Overview of the system architecture including the surgical console (master) and surgical robot (slave) connected through a communication layer with three different options that were studying as part of the experimental evolution of the system (see Sect. 8.4)

connected to the Master PC via USB. Using a UDP protocol the position command is transmitted through the network layer to the remote site and received by the slave PC. Using the inverse kinematics, the position command is translated into joint command and sent via the D/A to the servo controllers. The servo controllers generate voltage commands to the DC actuators of the surgical robot which in turn move the robot to the commanded position. A video stream of the surgical site is first compressed in the remote site by either software or hardware and then stream through the network layer to the surgical console. In the surgical console, the video following its decompression is presented to the surgeon on a monitor. A foot paddle controlled by the surgeon allows to engage and disengage the master and the slave by activating the brakes. Indexing is the term describing the process in which the surgeon disengage from the robot, reposition the input devices, and reengaged with to robot to continue the operation. Indexing is enabled by brakes mounted on the motors of the robot, which fix the position and the orientation of the robot in space during the time when the robot is disengaged from the surgical console.

### 8.3.1 Surgical Manipulators

The seven-degree-of-freedom (7-DOF) cable-actuated surgical manipulator, shown in Fig. 8.5, is broken into three main pieces: the static base that holds all of the motors the spherical mechanism that positions the tool and the tool interface. The motion axes of the surgical robot are: (1) the shoulder joint (rotational); (2) the elbow joint (rotational) (3) tool insertion/retraction (translational) (4) tool rotation (rotational) (5) tool grasping (rotational) (6) tool wrist-1 actuation (rotational) (7) tool wrist-2 actuation (rotational).

The first four joint axes intersect at the surgical port location, creating a spherical mechanism that allows for tool manipulation similar to manual laparoscopy. The mechanism links are machined from aluminum, and are generally I-section shapes with structural covers. These removable covers allow access to the cable system, while improving the torsional stiffness of the links. The links are also offset from the joint axis planes, allowing for a tighter minimum closing angle of the elbow joint.

The RAVEN utilizes DC brushless motors located on the stationary base, which actuate all motion axes. Maxon EC-40 motors with 12:1 planetary gearboxes are used for the first three axes, which see the highest forces. The first two axes, those under the greatest gravity load, have power-off brakes to prevent tool motion in the event of a power failure. The fourth axis uses an EC-40 without a gearbox, and Maxon EC-32 motors are used for the remaining axes. Maxon DES70/10 series amplifiers drive these brushless motors. The motors are mounted onto the base via quick-change plates that allow motors to be replaced without the need to disassemble the cable system.

The cable transmission system comprises a capstan on each motor, a pretension adjustment pulley, various pulleys to redirect the cables through the links, and a termination point to each motion axis. The shoulder axis is terminated on a single partial pulley. The elbow axis has a dual-capstan reduction stage terminating on a partial pulley. The tool insertion/ retraction axis has direct terminations of the cables on the tool holder. The tool rotation, grasping, and wrist cables are terminated on capstans on the tool interface. The cable system transmission ratios for positioning the tool tip are as follows. (1) Shoulder: 7.7:1 (motor rotations:joint rotations); (2) Elbow: 7.3:1 (motor rotations:joint rotations); (3) Insertion: 133:1 (radians:meters).

Each axis is controlled by two cables, one for motion in each direction, and these two cables are pre-tensioned against each other. The cables are terminated at each end to prevent any possibility of slipping. The cable system maintains constant pretension on the cables through the entire range of motion. Force and motion coupling between the axes is accommodated for in the control system.

Laser pointers attached to the shoulder and elbow joints allow for visual alignment of the manipulator relative to the surgical port. When the two dots converge at the port location, the manipulator is positioned such that its center of rotation is aligned with the pivot point on the abdominal wall. The power-off brakes can be released by flipping a switch located on the base. The brakes are normally powered by the control electronics, but also have a battery plug-in for easy set-up and breakdown when the system is not powered. ABS plastic covers were created on a three-dimensional printer to encapsulate the motor pack thereby protecting actuators, encoders and electrical wiring. Figure 8.11b shows the complete patient site.

## 8.4 Experimental Evaluation

The methodology is divided into two sections: field experiments and lab experiments that were performed with Raven [24–27, 38–43]. The field experiments were used in part to define latencies associated with different configurations of



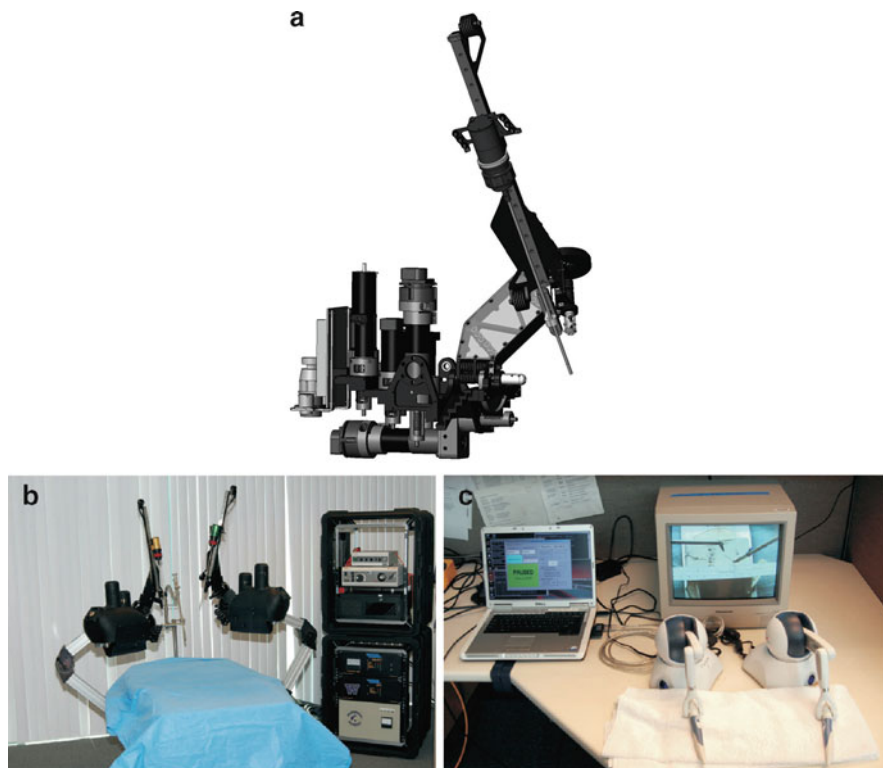


**Fig. 8.11** (a) RAVEN-Surgical Robotic system. CAD rendering of surgical manipulator shown with plastic covers removed. (Mass: 12.3 kg folded dimensions  $61 \times 53 \times 38$  cm extended dimensions:  $120 \times 30 \times 38$  cm. (b) The RAVEN patient site (Slave) and (c) the surgeon site (Master)

network architectures. Based on this information discrete and fixed time delays were selected and emulated in controlled lab experiments.

#### 8.4.1 Preliminary Experimental Evaluation

An adjustable passive aluminum mock-up was fabricated to model the kinematics of the spherical manipulator in parallel and serial configurations (Fig. 8.12 c, d). The mock-up was designed such that a real MIS tool with a 5 mm shaft could pass through the distal joint and allowed for varying the link angles (angles between Joints 1 and 2, and 2 and 3). In a dry-lab set-up, a number of kinematic configurations were compared utilizing a plastic human torso used for training (Simulab, Seattle, WA) to assess range of motion and potential collision (Fig. 8.12a, b). The results indicated that the parallel configuration had a limited workspace with kinematic singularities contained within that workspace (Fig. 8.12a). It was found that mechanisms with large link angles were subject to robot–patient collisions.



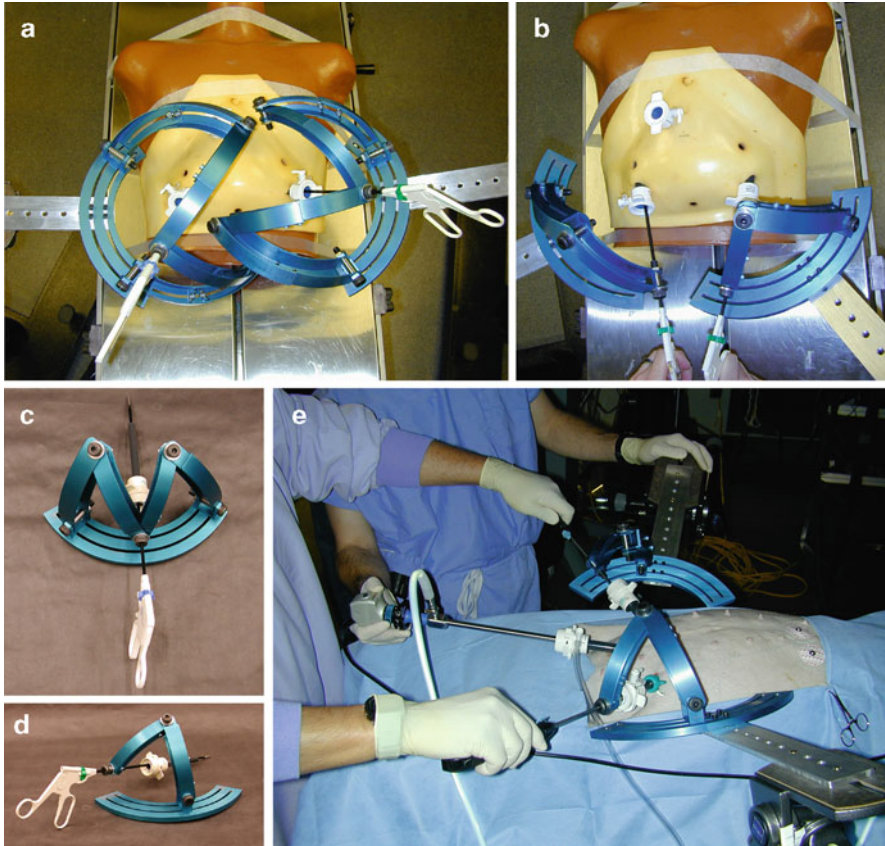


**Fig. 8.12** Aluminum Mock-up with adjustable link length and base length. The surgical endo-scopic tool is inserted into a guide located at mechanism apex in a configuration that allow to test different design candidates in a real minimally invasive surgical setup. (a) Parallel Configuration (b) Serial Configuration (c, d) Two configurations tested in a MIS setup. (e) Testing the make up in an animal lab. Although the robot manipulator will be teleoperated, in this evaluation the surgeon guides these passive mock-ups in order to evaluate the range of motion

Using two parallel mechanisms created potential self-collisions and constrained the distance between the two mechanisms, even with the link angles chosen as small as possible. Similar problems and constraints were observed for a hybrid configuration with a combination of one serial and one parallel mechanism. The best performance in terms of avoiding self-collision and robot–patient collision was achieved with both mechanisms in serial configuration (Fig. 8.12b).

Using two serial configurations in an experimental surgery with an animal model, surgeons confirmed that the serial 2-link with the dimensions given by the analytical optimization provided sufficient range of motion and did not suffer from self-collision, robot–robot collision, or robot–patient collision during both gross and dexterous manipulations (Fig. 8.12e).

## 8.4.2 Field Experiments

### 8.4.2.1 Field Experiments

Seven field experiments were conducted with Raven with various network architectures (wired and wireless) and a wide spectrum of physical distances (Table 8.4). In experiment No. 1 (HAPs/MRT) the system was deployed in two remote sites in desert-like conditions in Simi Valley, CA, while utilizing an Unmanned Aerial Vehicle (UAV) as a wireless node between the sites. In Experiment No. 2, (Imperial College London Collaboration), 6 (Surgical Robot Summer School) and 7 (Tokyo Tech Collaboration), the surgical robot located in Seattle was teleoperated from different sites around the world using commercial internet. In experiments 4 and 5 the surgical robot was deployed in the Aquarius – an undersea habitat, located 3.5 km off-shore in the Florida Keys, and teleoperated from Seattle, WA as well as the National Undersea Research Center, at Key Largo, FL using a combination of wired and wireless communication as part of NASA’s NEEMO (NASA Extreme Environment Mission Operations) 12 mission (Fig. 8.13).

### 8.4.2.2 Lab Experiments

#### System Setup

In a real teleoperation, physical distance and a real network separate the patient and surgeons sites with time varying delays (Fig. 8.14). When a surgeon makes a gesture using the master device, motion information is sent through the network to the Patient Site with a network time delay ( $T_n$ ). The manipulator moves and the

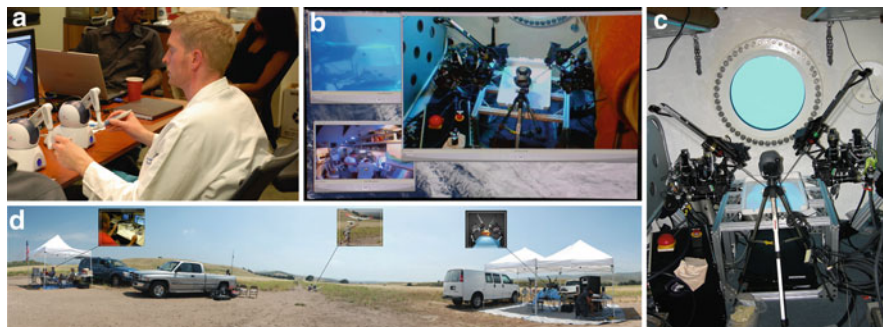


**Fig. 8.13** Field Experiments – Image Gallery (a) The surgical console (b) Overview of the surgical site as it is presented to the surgeon during the NEEMO 12 mission (c) Raven located in AQUARIUS during the NEEMO 12 mission (d) Panoramic view of the of the HAPs/MRT experimental setup

Table 8.4 Summary of field experiments with Raven

No.	Acronym	Patient site (Slave) surgical robot	Surgeon site (Master) surgical console	Communication layer video	Communication layer network architecture	Time delay (ms) <sup>(a)</sup>	Distance (km)
1	HAPs/MRT	Field – simi valley, CA	Field – simi valley, CA	HatVision, Hai560	Wireless via UAV	16	0.5
2	ICL	Seattle, WA	London, UK	iChat/Skype	Commercial internet	172	7,700
3	Animal Lab	Seattle, WA	Seattle, WA	Direct S-Video	LAN	1	0
4	NEEMO 12 – Aquarius	Aquarius (underwater), Key Largo, FL	Seattle, WA	HatVision, Hai1000	Commercial internet – seattle WA to key Largo, FL microwave Comm. – Key Largo, FL to Aquarius	76	4,500
5	NEEMO 12 – NURC	NURC (land), Key Largo, FL	Seattle, WA	HatVision, Hai200	Commercial internet	75	4,500
6	Surgical Robot – Course	Seattle, WA	Montpellier, France	iChat/Skype	Commercial Internet	170	8,500
7	Tokyo Tech Collaboration	Seattle, WA	Tokyo, Japan	iChat/Skype	Commercial Internet	150	7,600

<sup>a</sup>The time delay refers to the latency in sending position commands between the master and the slave. The latency regarding the video transmission, compression and decompression was not recorded

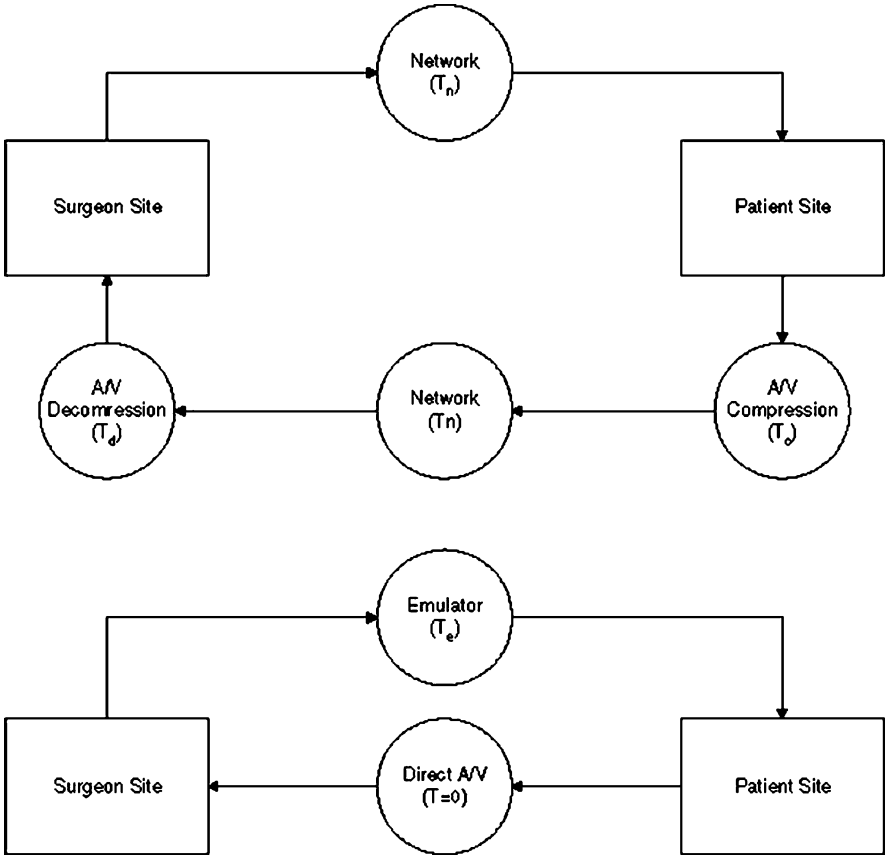


**Fig. 8.14** Simplified teleoperation communication flow. Real teleoperation in the field experiments (*top*) – Detailed diagram is depicted in Fig. 8.1. A setup for the lab experiments with emulated time delay (*bottom*)

audio/video (a/v) device observes the motion. Digital a/v is compressed ( $T_c$ ), sent from the Patient Site to the Surgeon Site through the network ( $T_n$ ), then decompressed ( $T_d$ ) and observed by the surgeon. The surgeon has experienced a total delay  $T = 2T_n + T_c + T_d$ , from the time (s)he made the gesture to the time that action was observed. In the simulated teleoperation the Surgeon and Patient sites are not separated by physical distance but are connected through a Linux PC with two network cards running NISTNET that emulates a real network. This emulator allows the experimenter to adjust the average packet delay between the Surgeon and Patient sites. The a/v feed is connected directly from the camera at the Patient Site to the monitor at the Surgeon Site through S-video eliminating any delay due to compression/decompression. The surgeon experiences a total delay,  $T_e$  due to the emulator, from the time (s)he made the gesture to the time that action was observed.

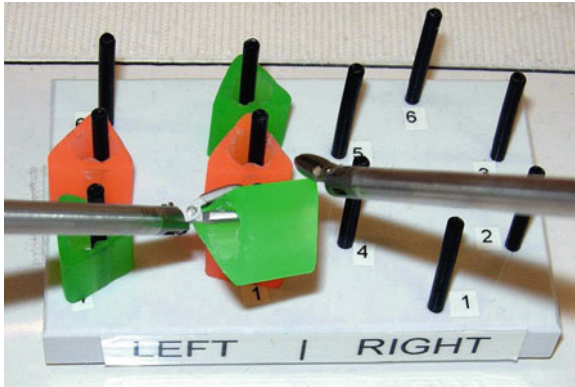


**Fig. 8.15** The Society of American Gastrointestinal and Endoscopic Surgeons (SAGES) Fundamental Laparoscopic Skill (FLS) Block Transfer task board set up with the RAVEN

### Experimental Design

The Society of American Gastrointestinal and Endoscopic Surgeons (SAGES) developed a curriculum for teaching the Fundamentals of Laparoscopic Surgery (FLS) which includes both cognitive and psychomotor skills. The skills assessment consists of five tasks. The FLS skills tasks have been validated to show significant correlation between score and postgraduate year and are considered by many the “gold standard” in surgical skill assessment. The Block Transfer is one out of these five tasks that emulate tissue handling and manipulation.

The experimental task consists of moving six blocks, one at a time, from the left side of the FLS peg board (Fig. 8.15) to the right side and back to the original position in a sequential predefined order (total of 12 transfers). In our experiment, the completion time as well as the tool tip trajectory were recorded. The three treatments of the experiment included emulated delays of 0, 250 and 500 ms presented to the subjects in randomized order. Each experimental treatment was conducted three times by each subject (nine times total) in a randomized order.

The subjects performed the training tasks first with no delay then with 250 ms delay in order to learn how to teleoperate the RAVEN and minimize the learning effects during the execution of the experimental protocol. Within 1 week from the start of their training, they returned to perform the time delayed block transfer experiment.

### Subjects: Definition of the Population

Fourteen subjects, five surgeon and nine non-surgeons, ages ranging from 18 to 43, participated in this study under University of Washington Human Subjects Approval Number 01-825-E/B07.

### 8.4.3 Results

#### 8.4.3.1 Field Experiments

Given the stochastic nature of the network there is a specific distribution of packet delay. Figure 8.16 depicts the distribution of the delay during the NEEMO experiments given a transmission rate of 1 K. The distribution of the latency is in the range of 63–95 ms with a pick at 78 ms. Table 8.1 defines the average latencies during all the field experiments. One should note that these latencies represent only the delay in sending position command from the master to the slave ( $T_n$ ). The latency due to the digital a/v compressed ( $T_c$ ) and decompressed ( $T_d$ ) which is usually larger and hardware/software dependent and is estimated to be in the range of 200 ms (hardware compression/decompression) in the HAPs/MRT and about 1 s for the commercial internet (software compression/decompression).

Figure 8.17 summarizes the mean completion time for a single expert surgeon (E1) who participated in multiple field and lab experiments performing the block transfer task. In each of the first 3 weeks of training, E1 performed three repetitions of the Block Transfer in the lab environment with effectively no delay. There is a learning effect as E1's mean time improved from week to week. During the NEEMO mission E1 completed a single repetition of the task with the RAVEN in Aquarius and another single repetition with it on-shore in NURC Key Largo, FL. For comparison, E1, who uses a da Vinci clinically was able to complete the block transfer task in about 1 min using the da Vinci, taking only slightly longer with the stereo capability disabled.

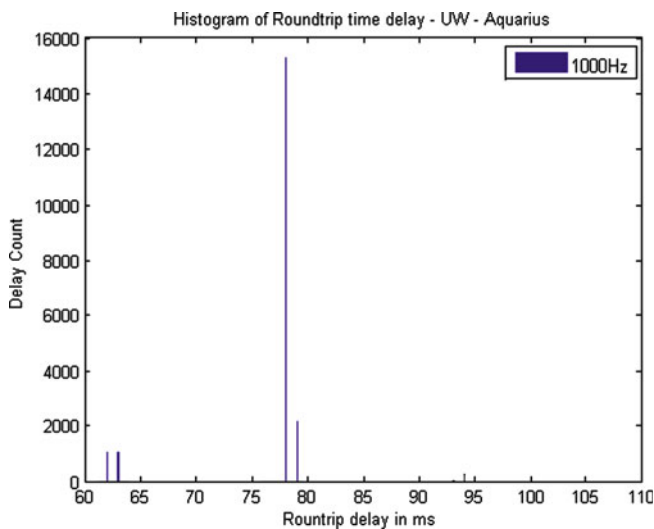


**Fig. 8.16** Histogram of number of packets with respect to delay between Seattle WA and Aquarius, Key Largo, FL at a transmission/receiving frequency of 1 K

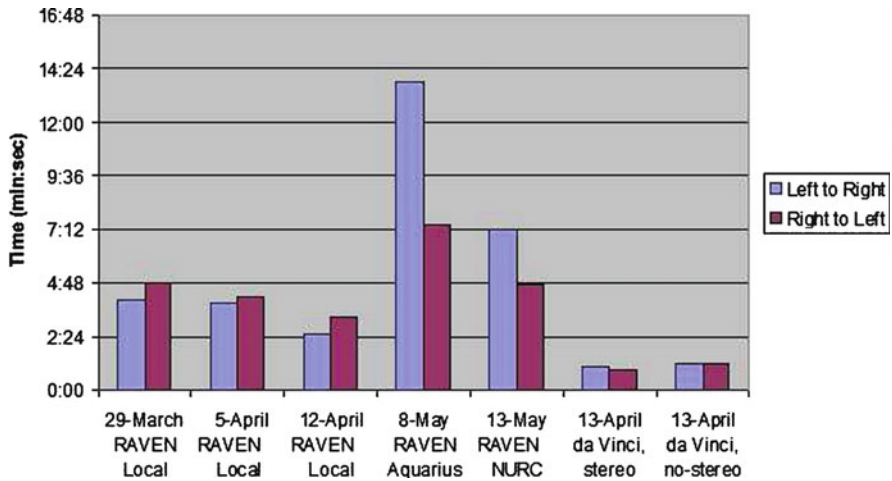


Fig. 8.17 Average block transfer completion times of a single expert surgeon during local training on the RAVEN as well as during the NEEMO mission. Completion times using an ISI da Vinci are included for comparison

### 8.4.3.2 Lab Experiments

A two-way analysis of variance (ANOVA) was used to determine the effect of the time delays (0, 250, 500 ms) and the subject group (surgeon, non-surgeons) on the three performance parameters: (1) block transfer completion time, (2) the number of errors (dropping the block – recovered and unrecovered); (3) tool tip path length as the response variables (time delays and group type). In general both the completion time and the tool tip trajectory length monotonically increased as the time delay increased (Fig. 8.18). The ANOVA analysis indicated that the difference in mean block transfer time as well as the tool tip path length between each of the three treatments (0, 250, and 500 ms delay) are statistically significant ( $\alpha < 0.02$ ) – Fig. 8.17. While the stated objective of the task was to minimize errors some errors occurred but the number of errors in response to delay effect and surgeon effect were not significant. It is possible that if the task was more technically challenging, the frequency or severity of errors would start to differentiate between subjects with more and less skill. The difference in mean block transfer completion time between surgeons and non-surgeons is not statistically significant.

## 8.5 Conclusion and Discussion

This chapter provides a comprehensive overview of the development, integration and the experimental evaluation of a surgical robotics system and its application in telesurgery.

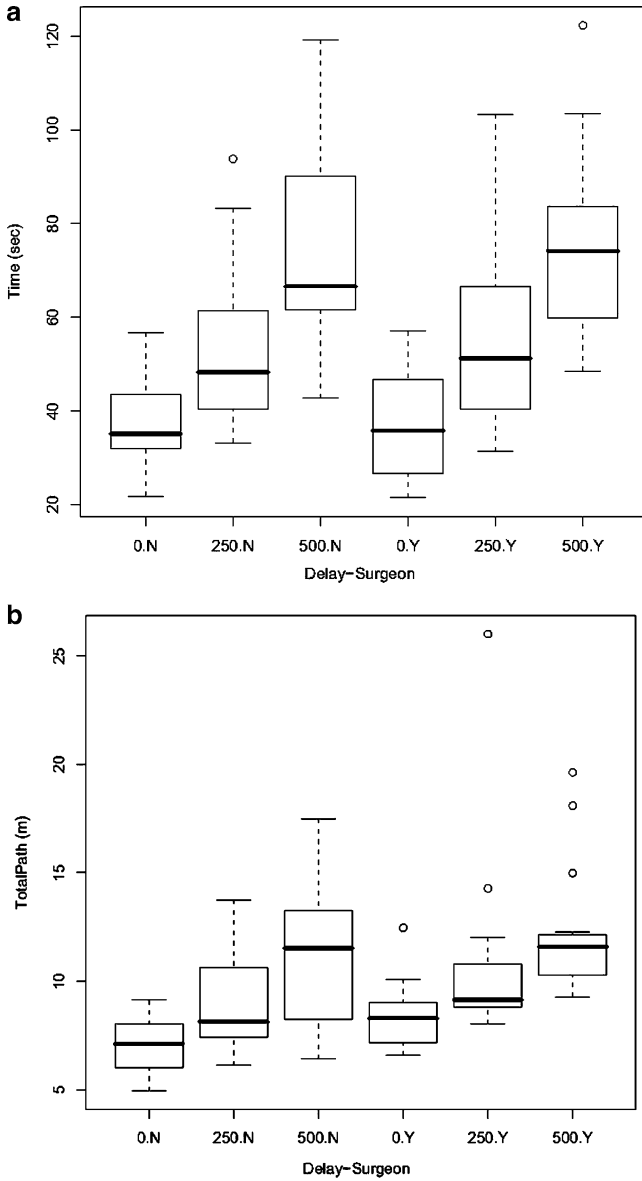


**Fig. 8.18** The effect of the block transfer completion time (a) and the tool tip path (b) are significantly different ( $\alpha < 0.02$ ) for the three time delays (0, 250, 500 ms), for both the surgeon (Y) and the non-surgeon (N)

The design of surgical robotic is based in part on transformation of clinical requirements that are translated to a set of quantitative specifications. The quantitative specifications for the surgical robot were obtained in part during in-vivo experiments with animal models and instrumented surgical tools. These specifications define the



workspace of the surgical tools along with and the loads applied on the tissues through the surgical tools in a MIS setup. The quantitative specifications enable a formal mechanism optimization that led to the smallest mechanism with the highest manipulability which meets the clinical requirements. As apart of the optimization process the kinematic equations of parallel, and serial spherical manipulators with link length angles less than  $90^\circ$ . The optimization cost function balanced a guaranteed minimum isotropy and summed isotropy over the target workspace with minimal total link length in order to yield a very compact, high-dexterity mechanism. Given the definitions of the DWS as the highly dexterous workspace and the EDWS as a reachable workspace associated with MIS, the parallel manipulator with the highest composite score had link angles of  $\alpha_{13} = \alpha_{24} = 52^\circ$  (Link 1) and  $\alpha_{35} = \alpha_{46} = 72^\circ$  (Link 2) and base angle  $\alpha_{12} = 0^\circ$ . Given the same constrains the serial manipulator with the highest composite score is the one with link angles of  $\alpha_{13} = 74^\circ$  (Link 1) and  $\alpha_{35} = 60^\circ$  (Link 2).

The base angle  $\alpha_{12}$  of the parallel manipulator has a profound influence on the workspace of the mechanism as well as its composite score. The reachable workspace of the parallel manipulator can be defined as the intersection of the workspaces of the left serial link and the right serial link arms acting as independent serial manipulators. When the base angle is zero, these two workspaces have a maximum overlap and therefore more space in which to place the required workspace cone that led to the highest performance score.

As the base angle,  $\alpha_{12}$  was varied from  $90^\circ$  to  $0^\circ$  the performance score first decreased, then increased, with a maximal value at a base angle of  $0^\circ$  and a minimal value at a base angle of  $70^\circ$ . In order to understand the relationships between the performance score as a function of the base angle, Link1 and Link2 were fixed at angle of  $60^\circ$  ( $\alpha_{13} = \alpha_{24} = \alpha_{35} = \alpha_{46} = 60^\circ$ ) and the base angle varied. A sequence of plots shows how the singular region that bisects the workspace moves with varying base angles (Fig. 8.8). When the base angle is  $90^\circ$ , the overlap between the odd and even sides is smaller, and the singular region is near the edge of the parallel workspace. Decreasing the base angle to  $45^\circ$  increases the overall workspace but moves the singular region more toward the middle of the workspace, thereby decreasing the usable workspace because the cone must not contain any singularities. Decreasing the base angle to  $0^\circ$  results in maximum workspace and moves the singularity down below the joint limits guaranteeing the reachable workspace that contains no singularities.

Optimization of the parallel mechanism shows that for a fixed base angle, better performance would be achieved by a mechanism design where the angle of Link2 is greater than that of Link1 ( $\alpha_{13} < \alpha_{35}$  and  $\alpha_{24} < \alpha_{46}$ ). Based on a spherical geometry, if Link2 is greater than Link1 and the base angle is 0, then the parallel mechanism cannot be put into a singular configuration.

The results for the serial mechanism showed good performance in a small form factor. For any serial design there exists a strip of maximum isotropy across the reachable workspace. This corresponds to a pose where  $\theta_3$  is some specific value and  $\theta_1$  can be varied. As the link lengths get larger the strip of best performance pushes away from the base (located at Joint 1), yet remains roughly centered in the overall workspace (Fig. 8.9b, d, f).

Fabricating passive aluminum mock-ups of the mechanism under study was critical to the evaluation of this class of manipulator for MIS applications. Through evaluation of various combinations of parallel and serial configurations, it was determined that two serial manipulators provide the smallest footprint and the fewest collisions in the common cases where two or more mechanisms occupy the limited space above the patient body. Based on the kinematic optimization, the link angles of these serial manipulators should be  $74^\circ$  for the first link and  $60^\circ$  for the second link. This configuration and design of manipulators results in the most compact mechanism that will perform MIS procedures with high dexterity in the entire workspace required.

The system integration of a surgical robot is an immense engineering effort that was resulted in an open architecture surgical robotic system that enables a wide spectrum of studies in surgical robotics and teleoperation. The chapter provides an overview of lab and field experiments studying the effect of time delay on surgical performance. A subset of a standard set of tasks (Fundamentals of Laparoscopic Surgery – FLS), which adopted by the MIS surgical community many surgical residency training programs was used in the majority of the field experiments and all the lab experiments. Block transfer emulating tissue handling along with suturing and knot tying defined the subset of the FLS that was adopted for the telerobotics experiments. Time delay is an embedded characteristic of any network. As indicated in the field experiments the latency related to the compression/and decompression of the audio/video (a/v) is significantly larger than the latency related to the transmission of position commands between the master and the slave. As such the a/v transmission latency is the limiting factor that determines the overall performance of the system. The results acquired in the lab experiments indicated a degradation of teleoperation performance characterized by increased completion time and tool path length, which were used as performance measures.

## 8.6 Visions

The premise of surgical robotics is to deliver high level of dexterity and enhance view of anatomical structures that is either too small or difficult to access (expose) for conventional surgical tools, the surgeons' fingers and a line of site. An approach to this anatomical structure may use either an open surgery technique, MIS or minimally access techniques that were otherwise. Aviation is often used a sources of inspiration for surgery. In both of these frameworks the pilot and the surgeon have to deal with complex system with high level situation awareness to communicate with additional individuals such as Co-Pilot and air traffic control personal in the aviation domain, and nurses (circulation nurse or sterile nurse) along with co-surgeons, and anesthesiologist in the surgery domain in addition to the immediate interaction with the system which is the airplane in aviation and the surgical site during surgery. Regardless of the many similarities between the two domains one should note that there is one fundamental difference between them. In aviation

the goal is to fly an airplane from point A to Point B with minimal interaction with the environment. However in surgery the goal is to change the environment (anatomical structure) in order to alter its function.

Although in small aircraft the pilot control the airplane through the stick which is analogues to a surgeon holding a surgical tool, automation is a concept that is widely used in a form of an automatic pilot in commercial and military airplanes. Automation in this context removes the human form the low-level operation (e.g. correcting a drift in the airplane flight path or manipulating the soft tissue due to deformation in surgery) and reposition the pilot or the surgeon as a high-level decision maker using supervisory control mode with interrupted intervention in critical steps of the operation.

With the introduction of a surgical robot automation in surgery can be implemented at two different levels: (1) system services and (2) surgical operation. The Trauma Pod project as envisioned by Dr. Richard Satava and its translation into practice as part of the a phase I DARPA project (see for details the chapter by Pablo Garcia) demonstrated that services to the surgical robot along with overall operating room (OR) management can be fully automated. The end-result was a fully automated operating room in which the only human in the OR may be only the patient. A centralized robotic surgical nurse provided services to the surgical robot such as tool dispensing from an automatic tool changer and changing, as well as equipment dispensing and disposing from an automatic equipment dispenser, vital signs monitoring, and overall supply chain management (inventory monitoring) – actions that took place upon voice command by a surgeon interacting with the surgical console.

As far as services to the surgical robot are concerned (tool change and equipment dispensing) centralized solution was used in a form of a single surgical nurse. As a result the performance of the entire system in providing these two services is dictated by the performance of the surgical nurse alone. An alternative approach in which each surgical robot is attached to another robotic arm in a micro–macro configuration, allows each surgical robot to be an independent unit that may serve itself (replacing it own tools and picking its own supplies) – Fig. 8.19. In this configuration the nurse function is distributed among all the robotics arms allowing each one to function autonomously.

The micro–macro approach to surgical robotics in which a gross manipulator carry a high dexterous manipulator is inspired by the human arm and hand in which the human arm serves as the gross manipulator positions the wrist in space for high dexterity manipulation by the hand. This approach may allow to design small and fast responding manipulator with high manipulability in a limited workspace which occupy only a subset of the surgical site (micro) and mount it on a land slow manipulator with a large workspace (macro). The macro manipulator may move the base of the micro manipulator in case it will sense the micro manipulator operates close to the edge of its workspace. The movement is obviously transparent to the surgeon who should not be involved nor aware of these adjustments of workspaces. This distributed architecture from the functional perspective may also allow to distribute the surgical robotics arm around the patients in a way that will avoid robot to robot collision.

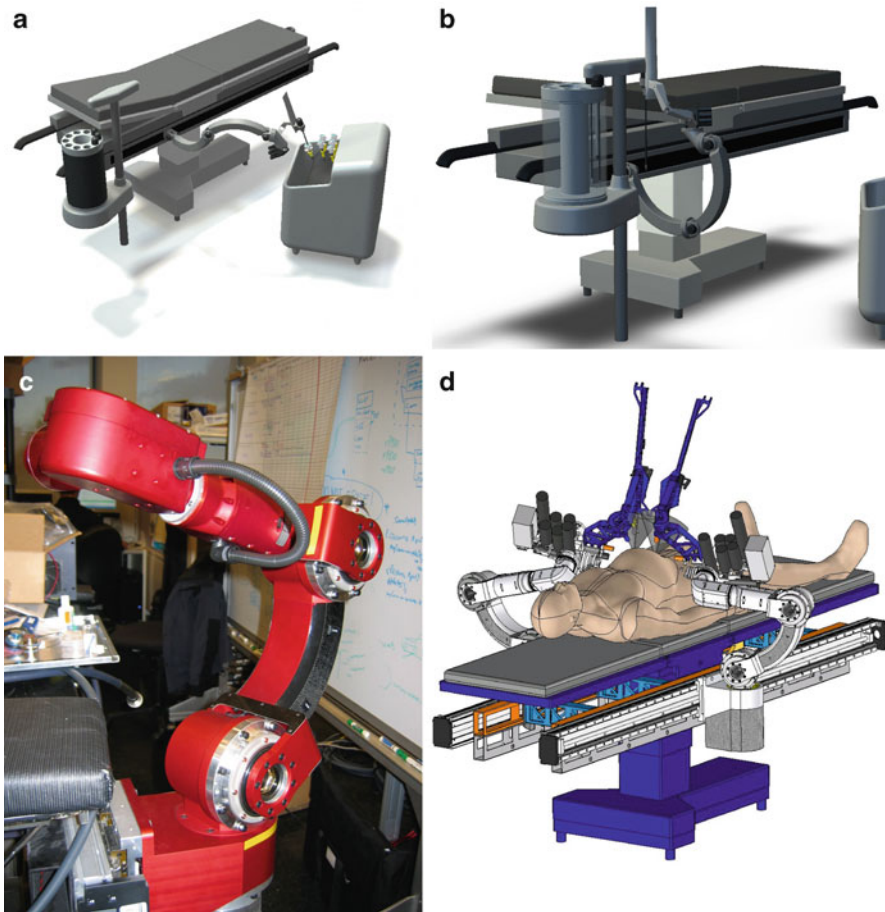


**Fig. 8.19** Distributed approach of automating services in the operating room. CAD rendering of a gross positioning arm (macro arm) carrying a surgical robotic arm (micro) replacing its own tool (a) or picking its own supply (b). A design of a macro arm named the “C-arm” (c). CAD rendering showing the Raven system (micro) carried by the C-arm (macro)

Automating the sub-tasks of the surgical procedure itself is another aspect that may contribute to the process in which the surgeons can be removed from his or her position of manually controlling the surgical robot to a position where he or she supervise the operation. In the context of tissue manipulation the surgeon may point to the target position and the robot will execute the command autonomously given constraints regarding obstacle avoidance and stress thresholds. One may envision a scenario in which the surgeon define the beginning and the end of the suture and the surgical robot operating in an autonomous mode stitch the tissue and tie a knot. One of the limiting factors to execute such a task autonomously is our limited capabilities in simulating and predicting the response of soft tissue to external loads. Once the robot interacts with the tissue its geometry changes significantly. Our limited

capabilities in predicting the soft tissue response are due to the non-linear, and un-isotropic nature of soft tissues. Another futuristic scenario may involve automatic edge detection and dissection of a tumor based on preoperative scans or biomarker that may be injected into the tissue.

Introducing a robotic system into the OR and utilizing such a system clinically was a major milestone for the field of surgical robotics. Emerging technologies based on scientific discoveries will continue to flow into the surgical robotic systems and provide better tool in the hands of the surgeons for delivering high quality healthcare.

**Acknowledgment** Development of the RAVEN was supported by the US Army, MRMC, grant number DAMD17-1-0202. The HAPs/MRT project was supported by the US Army TATRC, grant number W81XWH-05-2-0080. The surgical robot development was a collaborative team effort of students and faculty members in engineering and medicine who developed the system over the years including: Mitchell J.H. Lum (EE), Hawkeye King (EE), Diana C.W. Friedman (ME), Denny Trimble (ME), Thomas S. Lendvay (Children’s Hospital – Seattle), Andrew S. Wright (Surgery), Mika N. Sinanan (Surgery). The authors would like to thank the HAPs/MRT collaborators at the University of Cincinnati, AeroVironment, and HaiVision as well as our collaborators in London at Imperial College and at Tokyo Tech. The NEEMO XII participation has been supported by the US Army TATRC grant number W81XWH-07-2-0039. The authors would like to thank the NEEMO collaborators from University of North Carolina at Wilmington, US Navy, National Undersea Research Center, National Oceanographic and Atmospheric Administration, NASA, and in particular, Dr. Timothy Broderick, Charles Doarn, and Brett Harnett from the University of Cincinnati.

## References

1. Satava, R.: Disruptive visions: the operating room of the future, *Surg. Endosc.* **17**(1), 104–107 (2003)
2. Satava, R.M.: Surgical robotics: the early chronicles: a personal historical perspective, *Surg. Laparosc. Endosc. Percutan. Tech.* **12**, 6–16 (2002)
3. Satava, R.M.: Emerging technologies for surgery in the 21st century, *Arch. Surg.* **134**, 1197–1202 (1999)
4. Howe, R.D., Matsuoka, Y.: Robotics for surgery. *Ann. Rev. Biomed. Eng.* **1**, 211–240 (1999)
5. Buess, G.F., Schurr, M.O., Fischer, S.C.: Robotics and allied technologies in endoscopic surgery, *Arch. Surg.* **135**, 229–235 (2000)
6. Davies, B.: A review of robotics in surgery. *Proc. Instn. Mech. Eng.* **214**(H), (2000)
7. Clearly, K., Nguyen, C.: State of the art in surgical robotics: clinical applications and technology challenges. *Comput. Aided Surg.* **6**, 312–328 (2001)
8. Bloom, M.B., Salzberg, A.B., Krummel, T.M.: Advanced technology in surgery. *Curr. Probl. Surg.* **39**(8), 733–830 (2002)
9. Taylor, R.H., Stoianovici, D.: Medical robotics in computer-integrated surgery, *Robotics and Automation. IEEE Trans. Robot. Autom.* **19**(5) 765–781 (2003)
10. Lanfranco, A.R., Castellanos, A.E., Desai, J.P., Meyers, W.C.: Robotic surgery a current perspective. *Ann. Surg.* **239**(1), 14–21 (2004)
11. Louw, D.F., Fielding, T., McBeth, P.B., Gregoris, D., Newhook, P., Sutherland, G.R.: Surgical robotics: a review and neurosurgical prototype development. *Nuerosurgery* **54**(3), 525–537 (2004)

12. Speich, J.E., Rosen, J.: Medical robotics, In: Wnek, G., Bowlin, G. (eds.) *Encyclopedia of Biomaterials and Biomedical Engineering*, pp. 983–993. Marcel Dekker, New York (2004)
13. Binder, J., Bräutigam, R., Jonas, D., Bentas, W.: Robotic surgery in urology: fact or fantasy? *BJU Int.* **94**(8), 1183–1187 (2004)
14. Korb, W., Marmulla, R., Raczkowski, J., Mühlhng, J., Hassfeld, S.: Robots in the operating theatre – chances and challenges, *Int. J. Oral. Maxillofac. Surg.* **33**(8), 721–732 (2004)
15. Diodato, Jr, M.D. Prosad, S.M., Klingensmith, M.E., Damiano, Jr, R.J.: Robotics in surgery. *Curr. Probl. Surg.* **41**(9), 752–810(2004)
16. Camarillo, D.B., Krummel, T.M., Salisbury, J.K.: Robotic technology in surgery: past, present, and future. *Am. J. Surg.* **188**(Suppl to October 2004), 2S–15S (2004)
17. Curley, K.C.: An overview of the current state and uses of surgical robots. *Oper. Tech. Gen. Surg.* **7**(4), 155–164 (2005)
18. Kwoh, Y.S. Hou, J.L. Jonckheere, E.A., Hayall S.: A robot with improved absolute positioning accuracy for ct guided stereotactic brain surgery. *IEEE Trans. Biomed. Eng.* **35**(2), 153–161 (1988)
19. Takahashi, H., Warisawa, S., Mitsuishi, M., Arata, J., Hashizume, M.: Development of high dexterity minimally invasive surgical system with augmented force feedback capability. *Biomedical Robotics and Biomechanics, 2006. BioRob 2006*. In: *The First IEEE/RAS-EMBS International Conference on*, pp. 284–289 (2006)
20. Madhani, A.J. Niemeyer, G., Salisbury, Jr, J.K.: The black falcon: a teleoperated surgical instrument for minimally invasive surgery. In: *Proceedings of the Intelligent Robots and Systems*, vol. 2, pp. 936–944 (1998)
21. Cavusoglu, M.C. Tendick, F., Cohn, M., Sastry, S.S.: A laparoscopic telesurgical workstation. *IEEE Trans. Robot. Autom.* **15**(4), 728–739 (1999)
22. Marescaux, J.: Transatlantic robot-assisted telesurgery. *Nature* **413**, 379–380 (2001)
23. Marescaux, J. Leroy, J., Rubino, F., Smith, M., Vix, M., Simone, M., Mutter, D.: Transcontinental robot-assisted remote telesurgery: feasibility and potential applications advances in surgical technique. *Ann. Surg.* **235**(4), 487–492 (2002)
24. Rosen, J., Hannaford, B.: Doc at a distance. *IEEE Spectrum*, 34–38 (2006)
25. Sankaranarayanan, G., Hannaford, B., King, H., Ko, S.Y., Lum, M.J.H., Friedman, D., Rosen, J., Hannaford, B.: Portable surgery master station for mobile robotic surgery. In: *Proceedings of the ROBOCOMM, the first International, conference on Robot Communication and Coordination*, Athens, Greece, Oct 2007
26. Brett, H., Doarn, C., Rosen, J., Hannaford, B., Broderick, T.J.: Evaluation of unmanned airborne vehicles and mobile robotic telesurgery in an extreme environment, *Telemed. e-Health* **14**(6) 534–544 (2008)
27. Lum, M.J.H., Friedman, D.C.W., Sankaranarayanan, G., King, H., Fodero, II, K., Leuschke, R., Hannaford, B., Rosen, J., Sinanan, M.N.: The RAVEN – a multidisciplinary approach to developing a telesurgery system. *Int. J. Robot. Res. Special Issue: Medical Robotics Part I* **28**(9), 1183–1197 (2009)
28. Mitsuishi, M., Arata, J., Tanaka, K., Miyamotoamd, M., Yoshidome, T., Iwata, S., Hashizume, M., Warisawa, S.: Development of a remote minimally-invasive surgical system with operational environment transmission capability. In: *Robotics and Automation, 2003. Proceedings. ICRA'03. IEEE International Conference*, vol. 2, pp. 2663–2670 (2003)
29. Berkelman, P., Ji, M.: The University of Hawaii teleoperated robotic surgery system. In: *Intelligent Robots and Systems, 2007. IROS 2007. IEEE/RSJ International Conference on*, pp. 2565–2566, 29 Nov 2007
30. Berkelman, P., Ji, M.: A compact, modular, teleoperated robotic minimally invasive surgery system. In: *Biomedical Robotics and Biomechanics, 2006. BioRob 2006. The First IEEE/RAS-EMBS International Conference* (2006)
31. Rosen, J., Brown, J.D., Chang, L., Sinanan, M.N., Hannaford, B.: Generalized approach for modeling minimally invasive surgery as a stochastic process using a discrete Markov model, *IEEE Trans. Biomed. Eng.* **53**(3), 399–413 (2006)

32. Rosen, J., MacFarlane, M., Richards, C., Hannaford, B., Pellegrini, C., Sinanan, M.N.: Surgeon/Endoscopic Tool Force-Torque Signatures in the Evaluation of Surgical Skills During Minimally Invasive Surgery, *Studies in Health Technology and Informatics – Medicine Meets Virtual Reality*, vol. 62, pp. 290–296. IOS Press, Amsterdam (1999)
33. Rosen, J., Solazzo, M., Hannaford, B., Sinanan, M.N.: Objective Laparoscopic Skills Assessments of Surgical Residents Using Hidden Markov Models Based on Haptic Information and Tool/Tissue Interactions, *Studies in Health Technology and Informatics – Medicine Meets Virtual Reality*, vol. 81, pp.417–423. IOS Press, Amsterdam (2001)
34. Rosen, J., Brown, J.D., Barreca, M., Chang, L., Hannaford, B., Sinanan, M.N.: The Blue DRAGON – a System for Monitoring the Kinematics and the Dynamics of Endoscopic Tools in Minimally Invasive Surgery for Objective Laparoscopic Skill Assessment, *Studies in Health Technology and Informatics – Medicine Meets Virtual Reality*, vol. 85, pp.412–418. IOS Press, Amsterdam (2002)
35. Rosen, J., Brown, J.D., Chang, L., Barreca, M., Sinanan, M.N., Hannaford, B.: The blue DRAGON – a system for measuring the kinematics and the dynamics of minimally invasive surgical tools in-vivo. In: *Proceedings of the 2002 IEEE International Conference on Robotics & Automation*, Washington DC, USA, 11–15 May 2002
36. Rosen, J., Chang, L., Brown, J.D., Hannaford, B., Sinanan, M.N., Satava, R.: Minimally invasive surgery task decomposition – etymology of endoscopic suturing, *studies in health technology and informatics – medicine meets virtual reality*, vol. 94, pp. 295–301. IOS Press, Amsterdam (2003)
37. Taylor, R.H., Paul H.A., Brent, D., Mittelstadt et al.: Robotic Total Hip Replacement in days. *Proc 11 th IEEE Medicine & Biobgy Conft.* pp. 887–892, Seattle, 1989
38. Lum, M.J.H., Rosen, J., King, H., Friedman, D.C.W., Donlin, G., Sankaranarayanan, G., Harnett, B., Huffman, L., Doarn, C., Broderick, T., Hannaford, B.: Telesurgery via unmanned aerial vehicle (UAV) with a field deployable surgical robot. In: *Proceedings of Medicine Meets Virtual Reality (MMVR 15)*, pp. 313–315, Long Beach CA, 6–9 Feb 2007
39. Lum, M., Friedman, D., King, H., Donlin, R., Sankaranarayanan, G., Broderick, T., Sinanan, M., Rosen, J., Hannaford, B.: Teleoperation of a surgical robot via airborne wireless radio and transatlantic internet links. In: *The 6th International Conference on Field and Service Robotics*, Chamonix, France, 9–12 Jul 2007
40. Lum, M.J.H., Friedman, D.C.W., Sankaranarayanan, G., King, H., Wright, A., Sinanan, M.N., Lendvay, T., Rosen, J., Hannaford, D.: Objective assessment of telesurgical robot systems: telerobotic fls, medicine meets virtual reality (MMVR 16) pp. 263–265, Long Beach CA, Jan 29–Feb 1 2008
41. Lum, M.J.H., Rosen, J., Lendvay, T.S., Wright, A.S., Sinanan, M.N., Hannaford, B.: Tele-Robotic fundamentals of laparoscopic surgery (FLS): effects of time delay – pilot study. In: *30th Annual International Conference of the IEEE Engineering in Medicine and Biology Society EMBS*, pp. 5597–5600, Vancouver, British Columbia, Canada, 20–25 Aug 2008
42. Lum, M.J.H., Rosen, J., Lendvay, T.S., Sinanan, M.N., Hannaford, B.: Effect of Time Delay on TeleSurgical Performance. In: *IEEE International Conference on Robotics and Automation*, Kobe, Japan, 12–17 May 2009
43. Lum, M.J.H., Rosen, J., King, H., Friedman, D.C.W., Lendvay, T., Wright, A.S., Sinanan, M.N., Hannaford, B.: Teleopeartion in Surgical Robotics – Network Latency Effects on Surgical Performance. In: *31th Annual International Conference of the IEEE Engineering in Medicine and Biology Society EMBS*, Minneapolis MN, Sept 2009